TECHNISCHE
UNIVERSITÄT
WIEN
Vienna University of Technology

Diplomarbeit

Adhesion, Oxide Stability and Passivation Processes on Stainless Steel Bands

ausgeführt am Institut für Angewandte Physik
der Technischen Universität Wien

Im Zuge des Masterstudiums der Technischen Chemie, Synthesechemie

unter der Anleitung von
Univ.Prof. Dipl.-Ing. Dr.techn. Markus Valtiner
Laura Mears PhD
Dipl.-Ing. Lukas Kalchgruber BSc

durch

Michael Hahn, BSc

[redacted]

[redacted]

Monat 10, 2022

Unterschrift Student

Zusammenfassung

Wenn hochglanz-polierte Edelstahlbänder als Substrat für Polymerbeschichtungen verwendet werden, sind Adhäsionseigenschaften von zentraler Bedeutung. Im Detail geht es darum, Adhäsion quantifizieren und vergleichen zu können, um eine optimale Oberflächenbehandlung zu finden. Diese Arbeit verwendet SFA als analytisches Instrument, um adhäsive Drücke zwischen Modellproben von verschieden oxidierten Stahlbändern und SEBS-block-co-Polymer zu messen. Diese Messungen zeigen, dass sowohl eine thermische Oxidation, als auch ein Oxidation durch Plasmabehandlung die Ablöseeigenschaften verbessern, wobei die thermische Oxidation den größeren Einfluss hat. Komplementäre XPS-Messungen legen nahe, dass der Hauptgrund in der verringerten Materialdichte des Oxids an der Oberfläche und den deren Einfluss auf die Van-der-Waals Kräfte liegt, zeigen aber auch eine Korrelation mit der Hydroxy-Funktionalisierung der Oberfläche auf, was auf den Einfluss von H-Brücken schließen lässt. Oberflächenoxidation ist daher eine zielführende Methode, um die Ablöseeigenschaften im Stahl-Polymer System zu verbessern, wobei thermische Oxidation vor allem dann zu bevorzugen ist, wenn die Polymerstruktur über gute H-Brücken Akzeptoren verfügt.

Weiters treten auch bei hochglanzpolierten Edelstahlbändern bisweilen teure Korrosionsschäden auf. Um diese Angriffe im Detail zu verstehen, sind wir gefordert unsere analytischen Methoden ständig anzupassen und weiterzuentwickeln. Hier wurde eine etablierte Kopplung aus Elektrochemischer Durchflusszelle und ICP-MS neu adaptiert, um ein in-situ zerkratzen der Oxidschicht zu erlauben, und damit eine Messung der Repassivierung in Echtzeit. Erste Experimente bei OCP über verschieden Probenzusammensetzungen zeigen, unmittelbar nach Kratzen, einen exponentiellen Rückgang der präferenziellen Auflösung von Eisen, wenn die Probe repassiviert. Halbwertszeiten aus diesen exponentiellen Abnahmefunktionen könnten eine Möglichkeit bieten die Repassivierungsgeschwindigkeiten verschiedener Proben zu quantifizieren und zu vergleichen. Wenn diese Kratz-Experimente optimiert sind, versprechen sie interessante Rückschlüsse auf die Kinetik von Stahl-Repassivation in einem weiten Feld kontrollierbarer Parameter, wie Elektrolyt Komposition und Konzentration, sowie pH-Wert und angelegtem elektrischen Potential.

Abstract

When highly polished stainless steel bands are used as a substrate for polymer films the adhesive properties of the steel are a central point of interest. Specifically it is desirable to be able to quantify the adhesion, establish comparability and enable the selection of an optimal surface treatment. In this thesis the SFA was used as the main analytical instrument to quantify adhesive pressures of differently oxidized steel bands in a model system with SEBS as the polymer. It was found that both thermal oxidation and plasma treatment of the steels are beneficial for release properties, with thermal oxidation having the bigger impact. Complementary XPS results suggest the change in material density at the surface and its impact on van der Waals forces as the main reason, but also reveal a correlation of adhesive pressure with hydroxy-functionalization of the steel surface suggesting involvement of hydrogen bonding. Surface oxidation is therefore a sensible way to reduce adhesion in a steel-polymer system with thermal treatment being preferred – due to the lower percentage of hydroxy-functionalization – especially if the polymer structure includes strong hydrogen bond acceptors.

Additionally, even highly polished stainless steel bands are subject to occasional but highly costly corrosion damage. To understand these attacks we are incentivised to constantly adapt and expand our analytical toolset. Here, a preexisting electrochemical flow cell with ICP-MS coupling was redesigned and adapted to allow for in-situ scratching of steel samples, detecting a repassivation response in real time. Initial experiments performed at open circuit potential across a selection of sample compositions suggest an immediate exponential decay that follows a spike in the dissolution of the preferentially dissolved iron as the sample repassivates after the scratch. Half-life times determined from these scratches may give a way to quantitatively compare repassivation speed of different samples. Scratching experiments, once optimized, may give valuable insight into the kinetics of steel repassivation in a wide field of variable parameters such as electrolyte composition, concentration, pH, and electric potential.

Acknowledgements

I would like to thank Prof. Valtiner for the opportunity to work in his group – out of custom – and for his genuine interest in the work, his ceaseless optimism, and for handling a potentially stressful environment due all-our-favourite global pandemic in a calm, reasonable and flexible manner, because he really deserves it. To all the members of the group, thanks for friendly faces, which were rarer then, and helping hands, which tended to smell of disinfectant – but hey :).

Particularly, I want to mention: Lukas, a long-standing friend and my supervisor, for the corrosion part of the thesis. Whenever I work with you, it is a pleasure. Also you have gotten pretty good at chess, but don't tell anyone I said that. And Laura, who didn't have to involve herself with my work as much as she did and did it anyway, because she is passionate about what she does. Thank you for your remarkable patience and dedication to teach someone who knew absolutely nothing about SFA more that he really wanted to know. Also, I made good on my threat and hid a Rick-Roll in the thesis – don't look for it, you won't find it, I will show you sometime ;)

There are also some people working not directly in the group but in close cooperation with it that deserve thanks and recognition: Rainer Gärtner and Herbert Schmidt from the workshop and Heinrich Zlabinger from the electronics workshop, thank you for help and patience with a chemist in unfamiliar terrain.

I also need to thank my friend and flatmate Flo for kicking my ass when I was being lazy, and my friend Larissa for kicking my ass both more lovingly and more effectively regardless of whether I was being lazy or not.

Finally I would also like to thank my family for all the support I received so far; my dad for practical help and advice he gives me day to day and for having a great head to bounce ideas off, and my mum, for setting me up for success on my academic path from day one and every day since. Oh, and my brother I guess, although I'll be damned if I know what he contributed to the completion of this thesis. (Hab dich lieb Bruderherz, bin gespannt auf die Retourkutsche in deiner Arbeit!)

Contents

1. Introduction **1**
- 1.1. Thesis Motivation – The FunPak-Tribo Project 1
- 1.2. Goals of this thesis 2

2. Theoretical Part **4**
- 2.1. Adhesion 4
  - 2.1.1. Adhesive Forces 5
    - 2.1.1.1. Van der Waals Interactions 5
    - 2.1.1.2. Weak Hydrogen Bonding 6
  - 2.1.2. Static Equilibrium Contact Angle 6
    - 2.1.2.1. Surface Roughness 7
    - 2.1.2.2. The OWRK-Method 8
    - 2.1.2.3. Fitting a Linear Model 9
  - 2.1.3. Quantifying Adhesion – The SFA Approach 10
    - 2.1.3.1. The Surface Force Apparatus 10
    - 2.1.3.2. Why SEBS? 12
- 2.2. Corrosion 12
  - 2.2.1. Corrosion and Repassivation of Steel 13
  - 2.2.2. Electrochemical Flow Cell 15
  - 2.2.3. Electrode Reactions 15
  - 2.2.4. ICP-MS 16

3. Experiment Design and Instruments **17**
- 3.1. Chemicals 17
- 3.2. Contact Angle 18
  - 3.2.1. Experimental Setup 18
    - 3.2.1.1. Open Drop 18
  - 3.2.2. Sample Preparation 19
  - 3.2.3. Challenge of Directional Surface Roughness 20
- 3.3. SFA 21
  - 3.3.1. Optical Discs & PVD 21
  - 3.3.2. Spin-coating 22
  - 3.3.3. SFA – Hardware 24
  - 3.3.4. SFA – Software 24
  - 3.3.5. Sample Preparation 25
  - 3.3.6. Data Recording and Processing 26
    - 3.3.6.1. FECO Evaluation – SFA Explorer 26
    - 3.3.6.2. Force Evaluation 27

3.3.6.3. Newton Ring Evaluation 28
3.3.6.4. Roughness correction 29
3.4. Corrosion and Repassivation Experiments 31
3.4.1. Flow Cell 31
3.4.2. ICP-MS and Sample Preparation 32
3.4.3. Confocal Microscope 34
3.4.4. Samples 34
3.4.5. Electrochemistry 35
3.4.6. Data Evaluation 36

4. Results and Discussion **37**
4.1. Contact Angle Results 37
4.2. SFA – Adhesion 42
4.2.1. SFA Results 42
4.3. Corrosion and Repassivation Results 50
4.3.1. Iron-Chromium Model Samples 50
4.3.2. Dissolution Ratios 55
4.3.3. Multi-Element Samples 56

5. Summary and Outlook **58**
5.1. Contact Angle 58
5.2. SFA 59
5.3. Corrosion and Passivation 60
5.4. Overall Conclusion 61

References **62**

A. Adhesion Appendix **68**
A.1. OWRK diagram 68
A.2. Contact angle data 69
A.3. Contact angle missing error bars 70
A.4. Arduino Code 71
A.5. SEBS Refractive Index 72
A.6. SFA Calibration 73
A.7. SFA Long Time Experiment 74

B. Corrosion Appendix **75**
B.1. Calibrations 75
B.2. Mass Flows and OCPs 80
B.3. Unsmoothed ICP-MS Graphs 81
B.4. Dissolution Ratios 82

Abbreviations

A	Surface area
AES	Atomic emission spectroscopy
α_i	Standard error of data point i
b	Background signal
C	Constant depending on the type of pair potential
CCD	Charge-coupled device
CE	Counter electrode
CPS	Counts per second
D	Separation distance
ΔG_{ij}^{a}	Free Energy of adhesion per unit area for interfaces i,j
E_i	Expected data in data point i
EC	Electrochemistry
ESC	Electronic speed control
f	Degrees of freedom of the system
f_r, $\mathrm{f}_{20\%}$, f_{ges}	Roughness factors
FECO	Fringes of equal chromatic order
ICP-MS	Inductively coupled plasma mass spectrometer (spectrometry)
θ_y	Young contact angle
θ_w	Wenzel contact angle
Θ	Static equilibrium contact angle
k	Calibration constant (ICP-MS)
$\dot{m}$	Mass flow
MBI	Multiple beam interferometry
ν	Dissolution rate
O_i	Observed data in data point i
OCP	Open circuit potential
OWRK	Owens, Wendt, Rabel and Kaelble
$P_t, P_q, W_t, W_q, R_t, R_q$	Profile-, Waviness-, Roughness parameters (ISO 4287, DIN EN 180 4287)
PDMS	Polydimethylsiloxane
PVD	Physical vapor deposition
PWM	Pulse width modulation

π	Pi-electron system
r_{form}	Geometrical form factor (radius of curvature)
r	Roughness parameter
R	Sphere radius
RE	Reference electrode
ROI	Region of interest
ρ	Material density
SEBS	Styrene-ethylene-butylene-styrene blockcopolymer
SFA	Surface force apparatus
SHE	Standard hydrogen electrode
σ_i	Free energy per unit area for phase i
σ_{ij}	Free energy per unit area for interface i,j
σ_l^p, σ_l^d	Polar- and dispersive parts of the surface free energy of the liquid phase
σ_s^p, σ_s^d	Polar- and dispersive parts of the surface free energy of the solid phase
W_{ij}^a	Work of adhesion per unit area on the interface ij
W(D)	Work of adhesion as a function of separation distance D
WE	Working electrode
w(r)	Pair potential for interaction dependent on separation distance r
XPS	X-ray photo-electron spectroscopy
χ^2, χ^2_{red}	Chi-squared and reduced chi-squared parameters for fitting a linear model

1. Introduction

1.1. Thesis Motivation – The FunPak-Tribo Project

Mirror polished stainless steel bands are highly specialized products with a variety of application fields including automotive, food, film and foil, or laminate industries [1]. Careful attention for both production and application of such bands is given to the surface, with strict demands made for its properties and a strong interest to control them. If parameters are not well controlled, this can lead to a variety of problems, from costly corrosion damages on million-euro products to extreme stickage problems of polymer films when the bands are used as a substrate. To solve such problems, the surface properties can be changed – for example through oxidation, though different methods of oxidation may yield different results. It is therefore critical that we develop the analytical toolset to study both the problematic processes and the effects of surface modification introduced to alleviate the problems, to determine the best solutions.

Corrosion properties and adhesion properties are investigated in this thesis. Of these two, especially corrosion properties have been studied extensively in scientific literature. A lot of solutions were developed to answer specific corrosion problems ranging from altering the elemental composition of the materials, or the microstructure [2], to providing sacrificial anodes, [3] therefore we edge ever closer to a complete understanding of corrosion processes. Despite this new problems still arise and so does the need for analytical methods to study them.

The focus of this thesis regarding corrosion was the development of such a method, based on a three-electrode-electrochemical flow cell coupled with downstream ICP-MS detection. The novelty in this thesis was an adaptation of the cell design that allows for in-situ scratching of the sample-surface, making the repassivation process analytically accessible in real time. The scratching is accomplished by applying normal force to a rotatable seal with an eccentric sphere attached to it that scratches the surface, similar to setups commonly used in tribometers [4]. Alternative scratching modes were considered, but come with their own problems. Scratching from the side with a sliding motion instead of a rotation (as in [5]) makes it challenging to automate the process and to seal the cell, while forgoing the manual scratching in favour of a slurry-jet (as used in [6]) is incompatible with the downstream ICP-MS detection and limits the electrolytes. Similar scratching modes, using rotation, have also been tried in electrochemical cells on a much bigger scale, though not with ICP-MS coupling [7]. We hope to develop this technique to a point where it can provide unique insights into the kinetics of the repassivation process.

Apart from corrosion properties, the adhesive properties of the band's surface need to be tightly controlled. This is especially important when the bands are used as substrates for polymer foil that cannot be removed without stickage and residue if the adhesive energy in the system is too high. One common way to deal with adhesion problems would be anit-adhesion coatings [8,9]. Unfortunately, when the surface preparation, and specifically the polishing, are the main selling points of a product – as is the case for the studied steel bands – this option becomes, if not unfeasible, at least significantly less appealing. It is therefore both scientifically and economically interesting to find out which properties of surfaces give rise to high adhesion energies, to quantify, and to find out which processes can fine-tune these properties.

A second, equally important focus of this thesis, therefore, was the study of adhesive properties of the steel bands in steel-polymer systems. Here we focus mainly on different methods of oxidation and surface properties affected by them. The analytical technique employed to study these systems adds another, mainly scientific, note of interest to the topic. SFA, though commonly used to study phenomena related to adhesion, often relies on extremely flat samples. Acquiring interpretable, especially optical, information from a comparatively rough industrial steel samples – polished though it may be – can be viewed as a limit to testing in the context of SFA, and is definitely well outside the typical use-cases. In this thesis we hope to develop a steel-polymer model system based on the block co-polymer SEBS that allows for quantification and comparison. We hope to identify surface properties influenced by the oxidation of the steel samples that control adhesion in the system, and therefore a way to control the adhesive properties of the steel bands.

This thesis came to be as a result of the scientific collaboration between the Vienna University of Technology and Berndorf Band GmbH, sponsor and the industrial partner for this research.

1.2. Goals of this thesis

The goals of this thesis can be divided into two subsets of goals, for the study of corrosion and adhesion respectively.

The goals for the study of adhesion on oxidized steel bands were as follows:

- Establish that SFA is a viable technique for studying adhesion on rough surfaces

- Replicate contact angle experiments by Berndorf and compare results to the original as well as SFA results
- Investigate if a difference between different treatment methods (thermal/plasma-oxidation) can be found
- If there is a significant difference explain why

The goals for the study of corrosion on oxidized steel bands were the following:

- Develop, construct and test a new design for an electrochemical flow cell that allows for in-situ scratching of the sample
- Perform repassivation experiments with a large set of model-samples and samples of the industrial steels used by Berndorf, to study the repassivation behavior
- Explain differences, similarities, trends in the repassivation behavior and fit a model to the data

2. Theoretical Part

2.1. Adhesion

Many materials, when brought into reversible contact, resist separation – that is to say that some force is necessary to pull them apart, we need to invest energy. If the contacting bodies are different, this energy is the work of adhesion W^a which is the negative free energy of adhesion per unit area ΔG^a, related in Equation 1 [10]

$$\Delta G^a_{ij} = -W^a_{ij} = \sigma_{ij} - \sigma_i - \sigma_j, \tag{1}$$

with σ denoting the free energy per unit area for phases i, j and interface ij. For Equation 1 to describe a contact between solids they need to be flat and free of elastic strain [10]. The forces that cause adhesion are a variety of intermolecular interactions – all electromagnetic forces essentially, gravity being negligibly weak in the context of adhesion and the other two of the four elementary forces of nature, strong and weak interactions acting between elementary particles (such as protons, neutrons or electrons), being too short ranged. [11] Some space will be devoted to the discussion of some of these forces that are potentially relevant to the studied case in Section 2.1.1, but first a short but important side-note on units.

A problem with units may sometimes arise when measuring adhesion. With the surface force apparatus as a technique, for instance, the work of adhesion is not measured directly, but rather the force F(D) to pull two surfaces apart – the measurement result is in units of a force (commonly mN). This is typically converted into the desired units of a work of adhesion per unit area (W(D), also a function of the separation distance D) – which is equivalent to an adhesive force per unit length – using the Derjaguin approximation Equation 2 [11].

$$F(D) = 2\pi r_{form} W(D) \tag{2}$$

The geometrical factor r_{form} depends on the given rigid geometry of the system. In a sphere-on-flat contact – equivalent to the commonly used cross-cylinder configuration – r_{form} is the radius of the sphere [11]. For a non-rigid geometry there is a problem. To achieve comparable quantitative results this problem can be circumvented by normalizing by the contact area instead, obtaining the adhesion in units of an adhesive pressure (commonly mNmm^{-2}). Unfortunately there is no easy conversion between those two units and thus we cannot compare them. In the context of this thesis, as we are dealing with a non-rigid geometry, giving the results in units of adhesive pressure is proper.

2.1.1. Adhesive Forces

2.1.1.1. Van der Waals Interactions Consulting [11], types of intermolecular interactions we can expect to be relevant in our model system (adhesion of styrene-ethylene-butylene-styrene blockcopolymer (SEBS) on steel) are mainly van der Waals interactions and some weak hydrogen bonding, as there are no permanent charges present in the structure of the polymer, or the oxide layer of the steel, no medium other than air, and the polymer will not covalently bond to the oxide layer on contact.

Van der Waals interactions is a term for a group of interactions with pair potentials $w(r)$ proportional to r^{-6}. The three contributions are the Keesom energy (an interaction between two dipoles), the Debye energy (dipole — non-polar) and the dispersion energy (non-polar — non polar). It is important to note however, that while the interaction between macroscopic surfaces (in our geometrical setup a sphere and a flat surface) is based on these pair potentials, they are both qualitatively and quantitatively different and have a very different distance decay. Using the assumptions of additivity and that the pair potentials are purely attractive, Israelachvili [11] derives for van der Waals forces in a sphere-surface geometry the energy of equation 3

$$W(D) = -\frac{\pi^2 C \rho^2 R}{6D} \tag{3}$$

for the case of the separation distance D being much smaller than the radius of the sphere R; C is a constant depending on the type of pair potential. Note that the energy only decays as a function of $1/D$ – much more slowly than the pair potential it is based on. Understanding this difference is critical to explaining the relatively large distances of ~150 nm at which the attractive forces overwhelm the spring constant in the SFA and result in a jump into contact (see results Section 4.2.1). Further note the strong dependency on the material density ρ. The energy being smaller for less dense materials, such as the oxide layer compared to the bulk metal, leads to the expectation samples with thicker oxide layers will be less adhesive – an expectation well matched by the findings presented in 4.2.1.

2.1.1.2. Weak Hydrogen Bonding The second type of interaction we may expect to be relevant is hydrogen bonding. According to Israelachvili, H-bonding can be considered a purely electrostatic interaction, and no simple equation describing the pair potential exists, though the distance dependency is generally $\sim r^{-2}$ [11]. Considering the available functionalities in our model system, we note that the hydrogen bonds that could form

- O-H from the metal oxide as a donor with a π-acceptor in the polymer
- C-H from the polymer as donor with an O-acceptor in the oxide layer

are relatively weak in the context of hydrogen bonds. We can gauge the strength of these interactions by considering calculated H-bond energies of gas-phase dimers from [12] and references therein. It lists an Me-OH $\cdots$*benzyl* bond, which should be somewhat comparable to an Fe-OH$\cdots\pi$ interaction, at ~ 2.8 kcal mol^{-1} and a $CH_4\cdots OH_2$ interaction at $\sim 0.3 - 0.8$ kcal mol^{-1}, compared to hydrogen bonds for an interaction between two water molecules at ~ 5 kcal mol^{-1}. Estimating the impact of hydrogen bonding in our sample system on a macroscopic scale is much more difficult. Additivity can not really be assumed in the case of H-bonds because of their tendency for network formation [12]. Even though the potential for this is limited in our case, bifurcated, or even more complex configurations that have been observed with H-bonds may still occur.

2.1.2. Static Equilibrium Contact Angle

The static equilibrium contact angle is a characteristic physical property of a three-phase system of solid, liquid and vapor. Each such system has one defined angle Θ that reflects its equilibrium state, where the sum of all interfacial energies times their respective contact areas is a minimum and the vectorial sum of all forces in x-direction is zero (see Figure 1). This state is described by the Young Equation 4 for the static equilibrium contact angle , which can be derived from either this energy minimization or a force balance. A rigorous derivation can be found here [13].

$$\cos\theta_y = \frac{\sigma_{sv} - \sigma_{sl}}{\sigma_{lv}}, \tag{4}$$

where θ_y is the Young contact angle and σ denotes the surface free energy of the interfaces indicated by the indices s,l and v for solid, liquid and vapour respectively.

Measuring this contact angle is a way to characterize solid substrates with respect

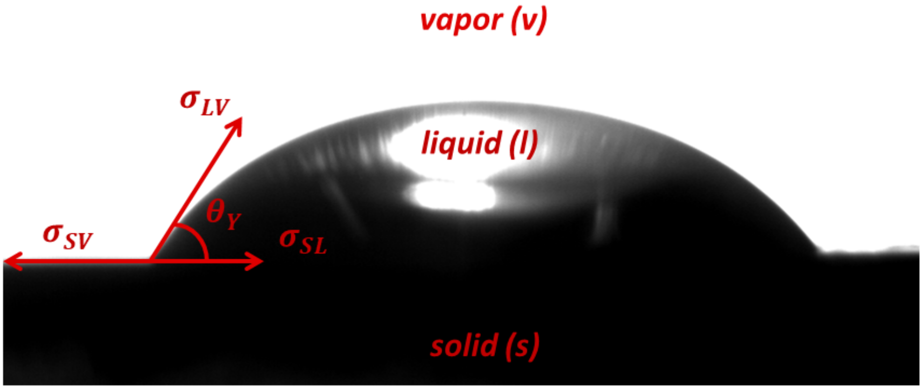

Figure 1: Illustration of the static equilibrium contact angle and the surface tensions involved. Indices denoting adjacent phases.

to their surface free energy, a parameter of interest when discussing adhesion. In this work specifically, the OWRK method 2.1.2.2 was employed to obtain additional information about the contributions of polar and dispersive forces to the total surface free energy. It is expected, considering the simple model presented in Figure 2, that in cases where there is a 'good overlap' – for example if both surfaces have a matching dominant dispersive or polar part (figure b) – a larger work of adhesion is observed than if there is a 'mismatch' (figure a).

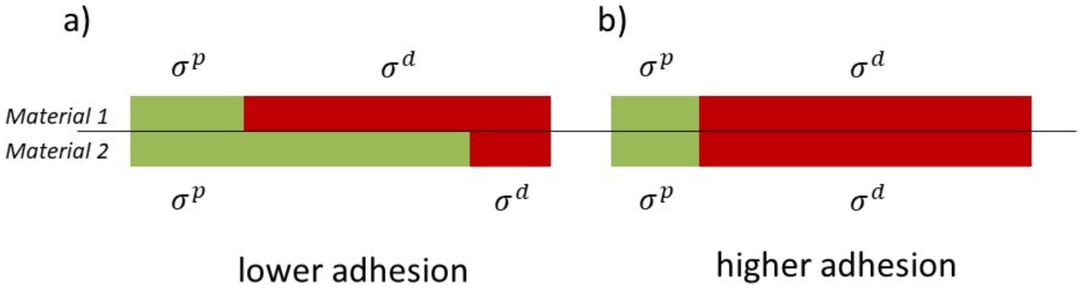

Figure 2: Two model cases illustrating worse a) and better b) matching polar and dispersive components of surface free energy, resulting in lower and higher adhesion.

2.1.2.1. Surface Roughness Surface roughness is a very influential parameter in contact angle analysis, as it directly influences the actual area contacted by the droplet. Many common effects are a product of, or strongly influenced by surface roughness, such as the lotus effect, superhydrophobicity in general or contact angle hysteresis [14]. In our case of the static equilibrium contact angle on steel, which is well below 90°, the stable state is described by the Wenzel model. The liquid is expected to fill pores and grooves on the surface thus contacting a larger than projected area resulting in better wetting compared to a smooth surface for contact angles <90°. To reflect this, the apparent contact angle – the Young contact angle θ_y – can be converted to the Wenzel contact angle θ_w by multiplying with a roughness parameter r, as in Equation 5.

$$\cos\theta_w = \frac{r * \sigma_{sv} - r * \sigma_{sl}}{\sigma_{lv}} = r * \cos\theta_y \tag{5}$$

$\theta_w < \theta_y$ follows from this equation for angles <90°, so applying this correction to the observed data will yield smaller contact angles that more accurately reflect the surface free energies present in the system.

Apart from the influence on the contact angle experiments, surface roughness also has a big influence on the SFA measurements. This is not usually a problem in SFA, as the technique is designed for and usually applied to molecularly smooth surfaces [11]. A way of dealing with the roughness in the SFA-experiments is presented in Section 3.3.6.4.

2.1.2.2. The OWRK-Method The OWRK-Method is a process for analyzing contact angle data developed by D. Owens, R. Wendt, W. Rabel and D.H. Kaelble [15–17]. The basic premise is a linearization of an equation published by D. Owens, R. Wendt in 1969 [15]. This linearized equation reads as follows, with the slope equal to $\sqrt{\sigma_s^p}$, the square root of the polar part of the surface free energy, and the intercept equal to $\sqrt{\sigma_s^d}$, the dispersive part.

$$\frac{\sigma_l(1+cos(\Theta))}{2\sqrt{\sigma_l^d}} = \sqrt{\sigma_s^d} + \sqrt{\sigma_s^p}\sqrt{\frac{\sigma_l^p}{\sigma_l^d}} \tag{6}$$

All solvents from which contact angles are measured on the surface of interest should lie on this linear function. It follows that only two solvents need to be used for recording contact angles. For ideal measurements this would then result in two data points which define a linear function from which the polar and dispersive parts of the surface free energy of the surface of interest can be calculated.

The parameters that have to be known are the polar and dispersive parts of the surface tension of the two test solvents, data that is taken from literature for the very common test solvents water and diodomethane, which have polar/dispersive components of 51/21.8 mJ/m², and 0/50.8 mJ/m² respectively [18].

In theory this is a very easy and neat method for evaluating the gathered contact angle data. In practice it becomes a little more complicated as the two ideal points split into two point clusters (see appendix A.1) because of error in repeat measurements and models for fitting the linear function need to be considered.

2.1.2.3. Fitting a Linear Model Probably one of the simplest and most widely used models that could be applied here is fitting the linear function with the least squares method (the sum of the squared residuals is minimized). Indeed this is the approach chosen by Berndorf in their initial experiment. One downside is that it does not include the error of each individual measurement point into the calculation. However it may sometimes prove necessary. A mathematical tool to handle this would be the chi squared approach, which includes the standard error for each data point, defined as in equation 7.

$$\chi^2 = \sum_i \frac{(O_i - E_i)^2}{\alpha^2}, \tag{7}$$

where O_i is the observed data set, E_i the expected data set and α_i the standard error of the data point i. The chi squared approach – at least in theory – allows for calculating the error propagation in the experiment. In practice this will turn out not to be possible, for reasons we will discuss in Section 4.1.

To judge the goodness of the fit, the reduced chi-squared parameter is employed, defined in equation 8

$$\chi^2_{red} = \frac{\chi^2}{f}, \tag{8}$$

where f is the degrees of freedom of the system calculated as the number of data points minus the number of parameters in the fit (in this case 2). Depending on the value of f, the null hypothesis should be questioned at different values of χ^2_{red}; in our case (f$\sim$ 10) at a value of $\chi^2_{red} > 2$ [19].

2.1.3. Quantifying Adhesion – The SFA Approach

Aside from the contact angle measurements it is desirable to quantify the adhesive pressure in a model system as close to the actual problem as possible – with a polymer and the steel actually in contact. In a surface force apparatus (SFA) we can investigate such a system. The instrument, as well as underlying principles of measurement will be discussed in the following Section 2.1.3.1.

2.1.3.1. The Surface Force Apparatus SFA is an optical technique based on multiple beam interferometry (MBI) that was first introduced by Tabor, Winterton, and Israelachvili (1968-1973) [20–22], and has since seen many iterations and improvements to expand the problem-space accessible with the technique [23–25] , among which the expansion allowing the operation in reflection mode [26] (and thus access to steel as a non-transparent sample) was particularly relevant for this thesis. Common uses today include measuring layer thicknesses, separation distances, contact radii and – the main interest in the context of this work – normal forces [27], allowing a quantitative analysis of adhesion. In fact, the first measurements of van der Waals forces – the main type of interaction we expect in our system – was performed using MBI in an SFA-setup [27, 28]. In the following section I will give a brief explanation of the technique, as a detailed discussion would exceed the scope of this thesis. Interested readers are invited to refer to these sources [23, 26, 29] and others for further details.

Figure 3 shows an SFA-setup operating in reflection mode.

The interferometer is formed by the flat, reflective steel sample, acting as a mirror, and a spherically capped optical disc made from fused silica and coated with semi-reflective Ti/Au layers (see Section 3.3.1), and a transparent polymer layer on top of that (see Section 2.1.3.2. In close proximity or contact an interference pattern can be observed at a selected wavelength; through a 532 nm filter for the Newton ring camera or with the spectrometer [1]) due to the varying distance with geometry (increasing outwards from the center of the spherical cap). The two surfaces can be moved in all three spacial directions respective to each other with micrometer screws and the separation distance in close proximity is precisely controlled by a piezoelectric actuator. One surface being mounted on a strain gauge

---

[1] Selecting one wavelength is necessary for clear interference patterns, as each wavelength corresponds to a different interference pattern which will overlap if poly-chromatic light is used. The choice of filter is usually not too important, unless the sample is strongly colored in the complementary color, which was the case for T1 – a deep red oxide layer – where a 580 nm filter was used instead.

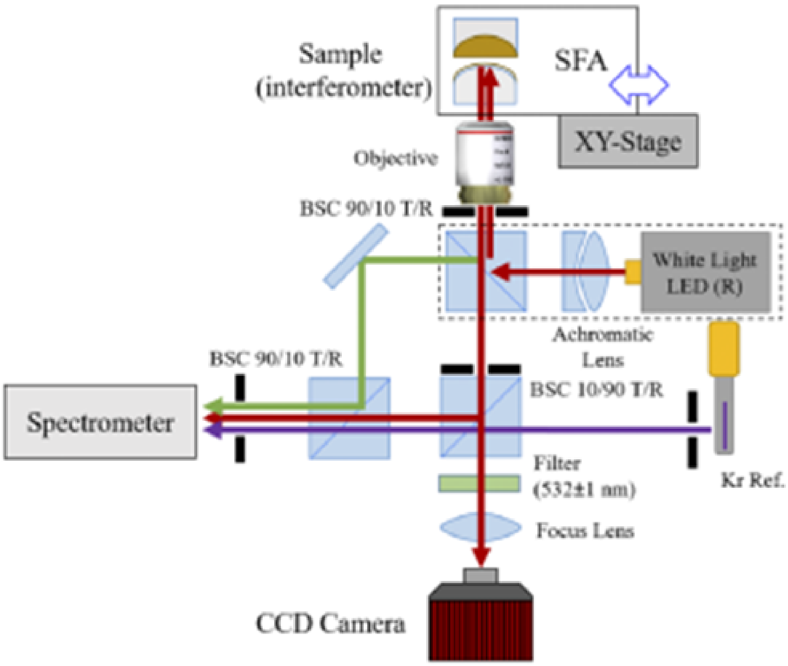

Figure 3: Schematic representation of an SFA working in reflection mode; graphic reused from [27] with permission; interferometer (top) is formed by spherically capped optical disc and the flat steel sample, acting as a mirror, instead of the depicted crossed-cylinder configuration. Green path = white light reference beam; purple path = krypton reference beam.

allows for normal forces to be recorded, while the bottom-view camera records the radially symmetric interference pattern (Newton rings) from that perspective and the slit/spectrometer setup records the fringes of equal chromatic order (FECO) – an alternative way of displaying the interference pattern by plotting the spacial coordinate of the spectral image over varying wavelength of light. This representation of the interference pattern, the FECO, are often a central point of interest in SFA-related research, as they contain a host of information about the system including layer thickness information, contact area information and information about separation distance. Accessing all this information is complicated (for a brief explanation see Section 3.3.6.1) using commonly employed atomically smooth mica layers, and much more so if significant roughness is involved (steel). Parts of the information encoded in the FECO – such as information about the contact area – may not be reasonably accessible anymore when working with very rough surfaces (compare Section 4.2.1), shifting emphasis onto the strain-gauge and Newton ring data.

2.1.3.2. Why SEBS?

For quantifying adhesion of a test polymer on the steel samples in a model system using the SFA approach, a suitable polymer needs to be chosen. Desired properties are:

- transparent
- soft, elastic and sticky
- ability to adapt to the surface roughness of the steel and establish full contact
- Easily deposited in a several μm thin, even film onto the optical discs used in SFA (preferably through spin-coating)
- Reasonable solubility in a comment solvent for easy spin-coating and cleaning

Before introducing the polymer chosen for the application – styrene-ethylene-butylene-styrene blockcopolymer (SEBS) – it is worth mentioning another, more commonly used polymer that comes to mind when considering the requriements: polydimethylsiloxane (PDMS), which would have been a fine choice, but does have the slight disadvantage of requiring a curing step, whereas SEBS is ready to go as soon as the solvent used in spin-coating has evaporated. The amount of curing agent and time in the case of PDMS might also significantly influence the properties making results harder to reproduce.

In addition to checking the first two items on the list of desired properties, there is encouraging evidence in literature that SEBS can be spin-coated into thin films [30], and solubility studies have been performed, recommending cyclohexane as a suitable solvent with a satisfactory solubility [31].

The most contentious of the requirements is probably item three, the ability to conform to surface roughness and establish close contact. It is unclear to what extent this is true exactly, but SEBS (PDMS as well) is known to form a conformable close contact with flat substrates due to the low glass transition temperature of the ethylene-butylene block [32].

2.2. Corrosion

Corrosion has broader and narrower definitions including different material groups or focusing solely on metals, but is usually defined as a destructive transformation of the material due to a chemical or electrochemical reaction with its environment

[33,34]. In practice this mostly describes unwanted oxidation of a metal, impairing material properties. For the purposes of this thesis we limit the discussion to corrosion of steels.

2.2.1. Corrosion and Repassivation of Steel

Iron as a material is particularly prone to corrosion damage. This has two main reasons: Firstly, iron is a base metal and relatively easily oxidized (see standard reduction potentials in Equations 9a and 9b [35]).

$$\mathrm{Fe^{2+} + 2\,e^- \rightleftharpoons Fe} \qquad -0.447V \tag{9a}$$

$$\mathrm{Fe^{3+} + 3\,e^- \rightleftharpoons Fe} \qquad -0.037V \tag{9b}$$

Secondly, in contrast to other base metals that form effective passive layers on the surface, protecting the bulk material from corrosion damage, such as Ti or Al [36], the oxide layer formed on iron by atmospheric corrosion ("rust") is permeable for corrosive species and does not adhere well to the bulk material. Thus it does not provide an effective barrier to shield the bulk material from further corrosion [37]. With stainless steel samples this problem is somewhat circumvented, as a high enough Cr content – typically well over $10wt\%$, although corrosion inhibiting effects start much earlier at $\sim 4\%$ [38], enables the formation of an effective protective layer on the surface. In these rust layers Cr is mainly in the oxidation-state Cr^{3+} such as in the compounds $Cr(OH)_3, CrOOH, or FeCr_2O_4$ [39]. The thermodynamic stability of these oxide layers across potential- and pH-ranges can be judged by studying Pourbaix diagrams such as Figure 4, for an $Fe-Cr-Ni-H_2O$ system.

Various stability domains are depicted in the diagram, but not all of them are relevant for us. The following are relevant for our measurements: Fe_2O_3 (cr), $FeCr_2O_4$ (cr) or Fe (cr), as we work at room temperature and neutral pH. [41]. Note that the Pourbaix diagram from Figure 4 was made for pure water as an electrolyte. The presence of Cl^- in the 1mM NaCl used in our experiments may shift regions of stability as Cl^- is known to significantly impact corrosion on steel [42, 43]. We should however be well within the stability domain of Fe(cr) during the -1.3V step (-1.08 vs SHE) so that assuming somewhat comparable conditions after the return to OCP and the re-formation of a passive layer seems justified, provided the wait period is long enough and the dissolution stabilizes.

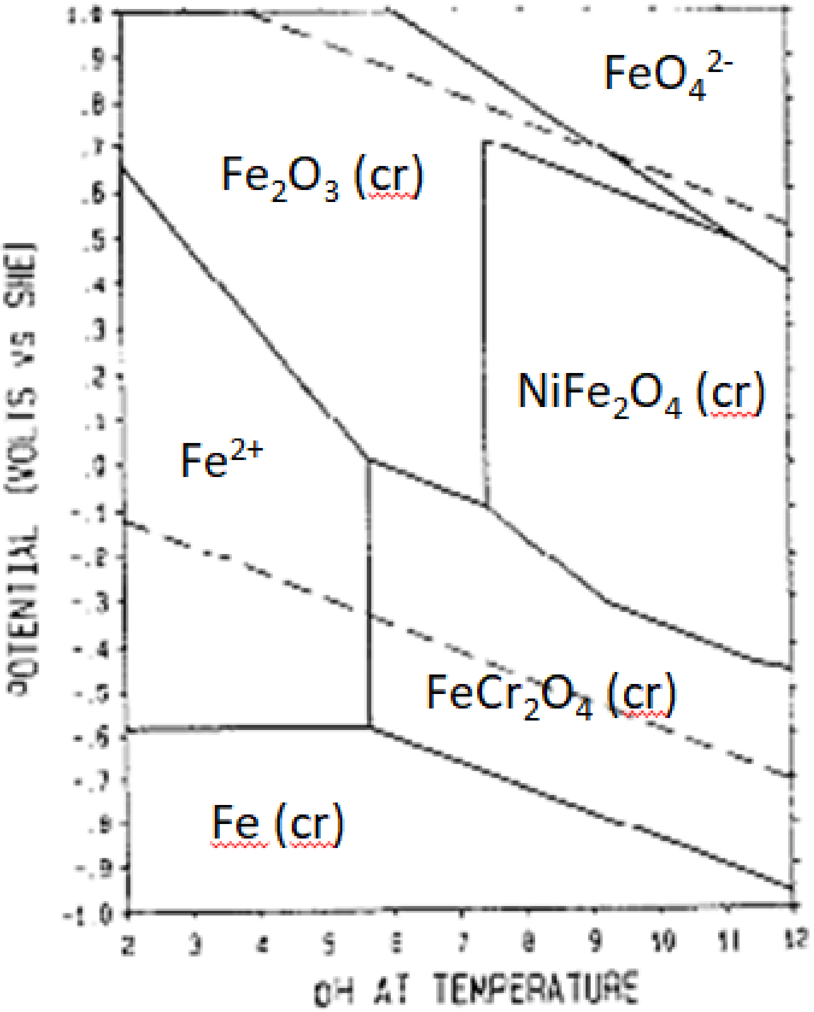

Figure 4: Pourbaix diagram of an $Fe - Cr - Ni - H_2O$ system at 298K with potentials given against the standard hydrogen electrode; graphic adapted from [40] with permission. Labels of stability domains rewritten for clarity.

In addition to chromium, molybdenum can also positively impact corrosion resistance [44], while nickel is added for improved mechanical properties and manganese to assist deoxidation and improve hardness [45].

2.2.2. Electrochemical Flow Cell

An electrochemical flow cell is a type of electrochemical cell that utilizes laminar flow over the working electrode to transport generated species away from the electrode helping to avoid diffusion limitation. The cell used for all the experiments in this thesis is discussed in more detail in Section 3.4.1. Briefly it has a three-electrode-setup consisting of a working electrode (WE), a counter electrode (CE) and a reference electrode (RE), where the potential is regulated between the working and the reference electrode while the current only flows between the working and the counter electrode, where electrochemical reactions occur. To limit the dissolution of the counter electrode it is made from a noble metal (in our case Pt). By excluding the reference electrode from the flow of current, momentary changes in concentration can be avoided, resulting in a more stable and constant potential [46]. For type of reference electrode there are several choices. The most well known and arguably most important reference electrode is the standard hydrogen electrode (SHE), which serves as a reference point for the electrochemical series. This same series however allows for easy conversion of potentials measured with other reference electrodes based on different redox pairs. In this thesis a Ag/AgCl reference electrode is used in all experiments (+0.22 V vs SHE), as it is much easier to handle in the experimental setup.

2.2.3. Electrode Reactions

On the reference electrode reactions given by Equations 10a and 10b occur:

$$\mathrm{Ag^+ + e^- \rightleftharpoons Ag\,(s)} \tag{10a}$$

$$\mathrm{AgCl\,(s) + e^- \rightleftharpoons Ag\,(s) + Cl^-} \tag{10b}$$

On the working electrode – the steel sample to be corroded – oxidation reactions take place, dependent on the applied potential (in this case OCP) and the element species; described in general terms by Equation 11.

$$\mathrm{M\,(s) \rightleftharpoons M^{\mathit{n}+} + ne^-} \tag{11}$$

Pourbaix diagrams help predict which reactions occur in specific cases. Consulting Figure 4 and our typical OCP values from Section B.2, we see that we are at a borderline case, with either $Fe_2O_3(cr)$, or $FeCr_2O_4(cr)$ being the stable species. Since this Pourbaix diagram is not perfectly applicable to our case as we don't use pure water as a solvent but rather a 1mM NaCl solution, either of the following two reactions given by Equations 12a, 12b may occur in the specific case of Fe.

$$\mathrm{Fe} \rightleftharpoons \mathrm{Fe}^{2+} + 2\,\mathrm{e}^- \tag{12a}$$

$$\mathrm{Fe} \rightleftharpoons \mathrm{Fe}^{+3} + 3\,\mathrm{e}^- \tag{12b}$$

The counter electrode is where the corresponding reductions occur when the working electrode corrodes. At OCP the expected counter-reaction is the hydrogen evolution reaction given by Equation 13.

$$2\,\mathrm{H}^+ + 2\,\mathrm{e}^- \rightleftharpoons \mathrm{H}_2 \tag{13}$$

2.2.4. ICP-MS

ICP-MS is an analytical technique that allows both qualitative and quantitative analysis of multiple elements. The (usually liquid) sample is pumped into the ICP-MS, dispersed into small droplets by a nebulizer and rapidly vaporized, atomized and ionized by the inductively coupled plasma. Ions can then be separated by their mass to charge ratio in a quadrupol mass analyzer. Advantages that make ICP-MS analysis suitable for coupling with an electrochemical flow cell are fast measurement times, multi-element detection and very high sensitivity with detection limits in the ppt-range and quantification limits in the ppm-range [47]. For these reasons, the coupling of ICP-MS with an electrochemical flow cell is an attractive tool, established in scientific literature [48]. Though the quantification potential is not fully used in the early experiments presented in this thesis, it is a big potential plus for more refined experiments in the future.

3. Experiment Design and Instruments

3.1. Chemicals

Table 1: Chemicals used in experiment: contact angle (CA), corrosion (ICP), surface force apparatus (SFA).

Chemical	**Experiments**	**Purity**	**Supplier**
Ethanol	CA, ICP, SFA	Gradient grade for chromatography	Sigma-Aldrich
H_2O	CA, ICP	Distilled and ion-exchanged $\rho \sim 18\text{M}\Omega$ cm	Milli-Q Reference A^+ System
CH_2I_2	CA	99%, Cu as stabilizer	Sigma-Aldrich
P_4O_{10}	CA	99%	Sigma-Aldrich
Cyclohexane	SFA	$> 99.9\%$	Carl Roth GmbH
SEBS	SFA	$< 1\%$ Antioxidant, av. M_w ~89.000 by GPC	Sigma-Aldrich
HCl	SFA	37%	Sigma-Aldrich
H_2SO_4	ICP, SFA	98%	Sigma-Aldrich
H_2O_2	SFA	50%	Carl Roth GmbH
NaCl	ICP	1mM Solution of $> 99.5\%$ NaCl in Milli-Q water	Sigma-Aldrich
HNO_3	ICP	65%	Merck KGaA
Ar	ICP	$\geq 99.999\%$	Air Liquide
N_2	ICP	$\geq 99.999\%$	Air Liquide
He	ICP	$\geq 99.999\%$	Air Liquide
$CaCO_3$	ICP	Precipitated for analysis	Sigma-Aldrich
Polishing solutions	ICP	MetaDi^{TM} Supreme	Buehler
Multielement standard	ICP	IV-Stock-10	Inorganic Ventures

3.2. Contact Angle

3.2.1. Experimental Setup

The experimental setup for measuring the contact angle, as depicted in Figure 5, consists of:

- A sample chamber with a pedestal in the center for the steel samples
- An inlet fitted into the lid, with tubing to connect to a syringe for the solvent
- A Thorlabs camera with a Edmund Optics 0.5×65 mm lens connected to a PC
- A bright LED lamp for backlighting

The camera is controlled with the Thorlabs software ThorCam version 3.5.1.1 and the pictures are evaluated using the open-source software OpenDrop 3.3.0-Windows. For analysis the OWRK-method is used as discussed in Section 2.1.2.2.

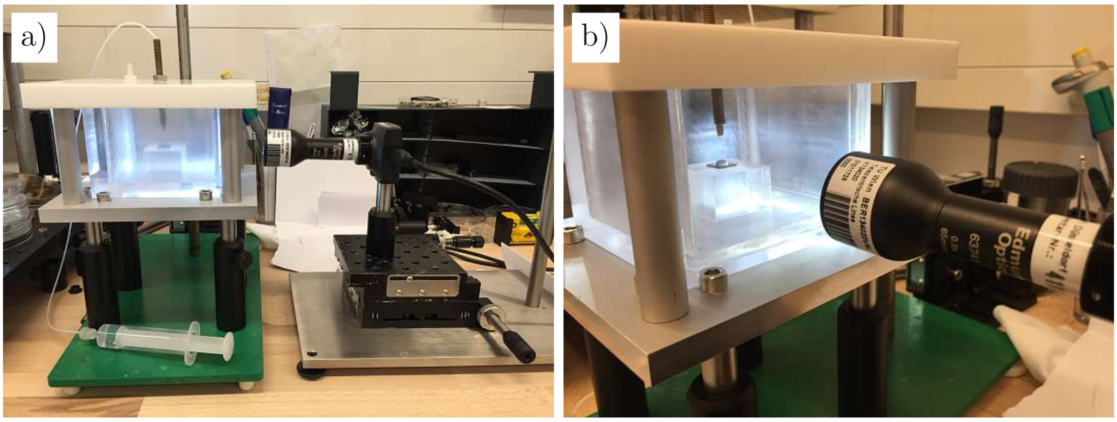

Figure 5: Contact angle experimental setup in side view a) and internal view b); Syringe for solvent input connected to the inlet fitted into the lid of the chamber; sample is placed on the pedestal in the chamber.

3.2.1.1. Open Drop Open Drop is an open-source contact angle processing software written in python [49]. It is completely free to use and available for various operating systems; in the context of this work the Windows-version of Open Drop

3.3.0 was used. Given sufficient image quality, the software is capable of automatically recognising the droplet-outline and calculating the contact angles on both sides, with the baseline the droplet is sitting on and a generous area of the image in which the droplet is located as the inputs. Figure 6 shows an example evaluation from our own data-set. For performance and reproducibility data for the software itself, please refer to the original literature [49].

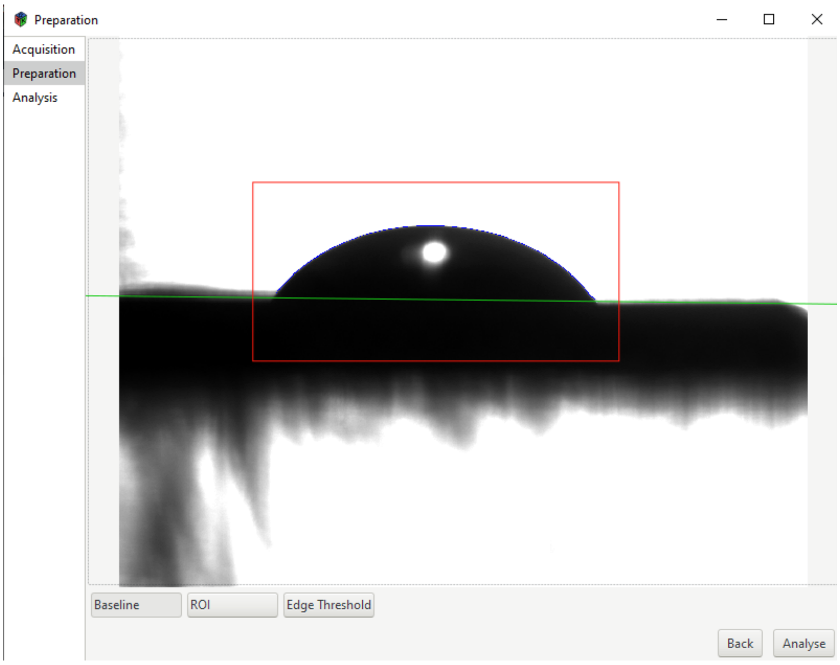

Figure 6: Example for contact angle evaluation with Open Drop. Input parameters: baseline (green) and ROI=region of interest (red); drop-outline (blue) recognized by the program.

3.2.2. Sample Preparation

The experiment's main purpose was to compare contact angles to measurements conducted by Berndorf Band on the same sample set. The sample preparation however was completely changed. In the original experiment the samples were simply dry-cleaned with a microfiber cloth. This was changed because the Berndorf method is unlikely to effectively remove residual oils on the steel that are present in the air and are adsorbed, as well as because of the potential residue from the protective foil that the steel was coated with for transport to prevent scratching.

A full list of the analysed samples is provided in Table 2; the set is the same as the set for the SFA-measurements. The samples, provided by Berndorf Band, were roughly 20 × 30 cm metal sheets with a thickness of ~2-3 mm. The protective polymer foil was removed and two ~ 2 × 2 cm platelets were cut from each of the samples. The samples were washed with ethanol and placed in ethanol in an ultrasonic bath for 20 min before every measurement cycle. Samples were then dried with a nitrogen-gun and measured immediately. This method however proved ineffective for the set using water as a solvent, where a trend towards smaller angles could initially be observed with repeat-measurements. The method of drying was therefore adapted to include a one hour period in a desiccator over phosphorus pentoxide immediately before measurement, which largely alleviated this problem.

Table 2: Summary of method of oxidation for individual samples.

Name	**Method of oxidation**	**Details**
T1	Thermally oxidized (oven)	505 °C, 90 min
T2	Thermally oxidized (oven)	300 °C, 10 min
T3	Thermally oxidized (oven)	300 °C, 30 min
T4	Thermally oxidized (oven)	300 °C, 120 min
T5	Thermally oxidized (oven)	400 °C, 30 min
P2	Plasma oxidized	Spacing high, high band velocity
P3	Plasma oxidized	Spacing low, low band velocity
P4	Plasma oxidized	Spacing high, low band velocity
P5	Plasma oxidized	Spacing low, high band velocity
REF	Reference sample	Natural oxide layer formation

3.2.3. Challenge of Directional Surface Roughness

One full set of measurements for a given solvent consisted of three repeat cleaning-cycles in which the two platelets for every sample were measured – six solvent droplets per sample and set – totaling 60 droplets per set. For each droplet four contact angles were recorded (left/right and left/right again after a 90° rotation of sample to counteract its directional roughness). This proved necessary because the contact angle was significantly influenced by the directional roughness being parallel or perpendicular to the optical axis (see Figure 7). This could even be observed by the naked eye, as some of the droplets were clearly not round but oval. The droplet was then described by the average of the four measured angles.

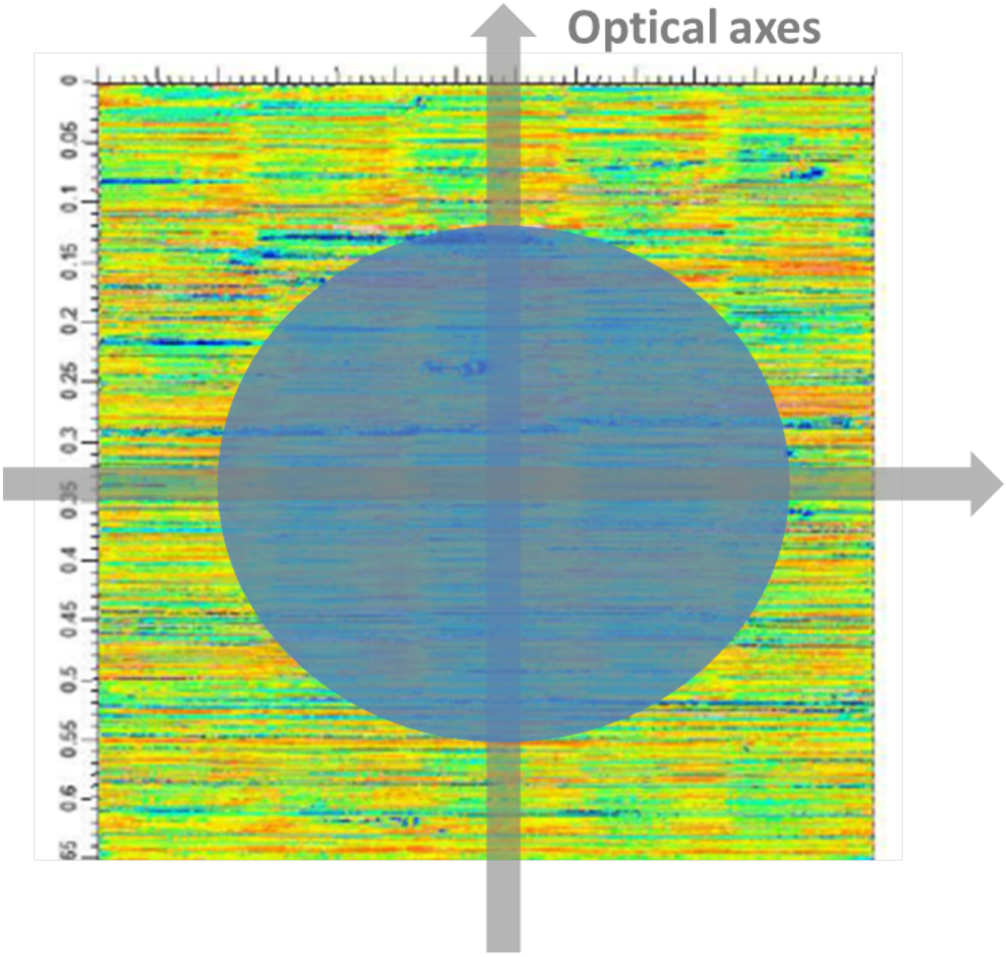

Figure 7: Schematic of the two optical axes used because of the irregular droplet shape; background is a height-colored confocal-microscope image showing the directionality of the surface roughness. Scale in mm, only applies to the background; Droplet not to scale, approximately on fifth of actual size.

3.3. SFA

3.3.1. Optical Discs & PVD

In the SFA experiment the steel is brought into contact with another surface which is prepared on a fused silica optical disc in the shape of a cylinder capped with a spherical dome with 2cm radius of curvature (Figure 8). The correct height is achieved by stacking the disc with another cylinder and gluing with a UV-hardening optically transparent glue (Norland Products, Optical Adhesive 81) in a teflon mold.

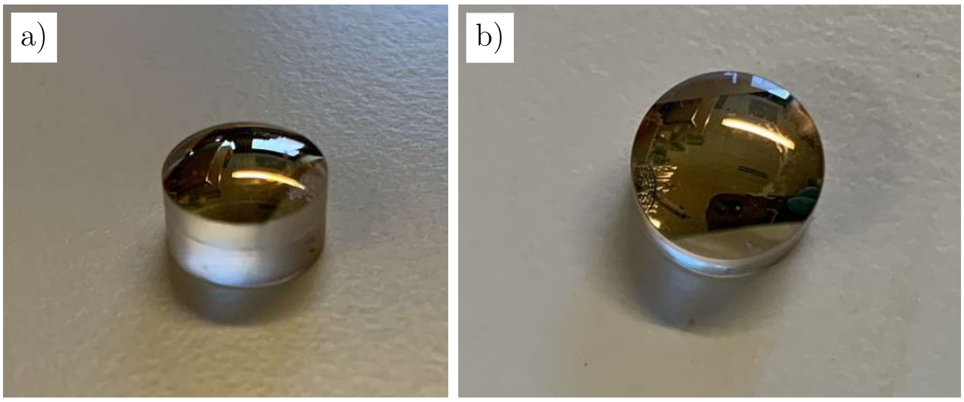

Figure 8: Pictures of the optical disc from different angles (coated); cylinder base and spherical cap with a 2 cm radius of curvature.

Before the optical discs can be used in SFA, a semitransparent, reflective layer needs to be deposited on the curved surface. Specifically ∼5 nm sputtered Ti at $< 9.8 * 10^{-3}$ mbar, followed by ∼40 nm of Au are deposited using physical vapor deposition (PVD) at a pressure of $\sim 5 \times 10^{-6}$.

3.3.2. Spin-coating

To further prepare the optical discs for contacting the steel sample in the SFA, they had to be coated with a several μm thin, homogeneous, smooth layer of SEBS polymer (see Section 2.1.3.2). To fulfill these requirements a spin-coating system was employed. This system was designed and built from scratch using a 2600 kV brushless DC drone motor and a custom made sample holder. To control the rotation speed of the motor, an Arduino circuit board was coded to regulate the motor via an electronic speed control (ESC), by varying the pulse length of the 50 Hz PWM-signal (pulse width modulation). The code is provided in appendix A.4. Assembly of the circuit closely followed a tutorial provided by Dejan at howtomechatronics.com [50] , with the exception of using a 230-12V adapter instead of batteries to provide the power. The sample holder was custom-made by the workshop at Vienna University of Technology for the optical discs used in SFA. Figure 9 depicts the circuit diagram, as well as the fully assembled setup, graphic adapted from howtomechatronics.com [50].

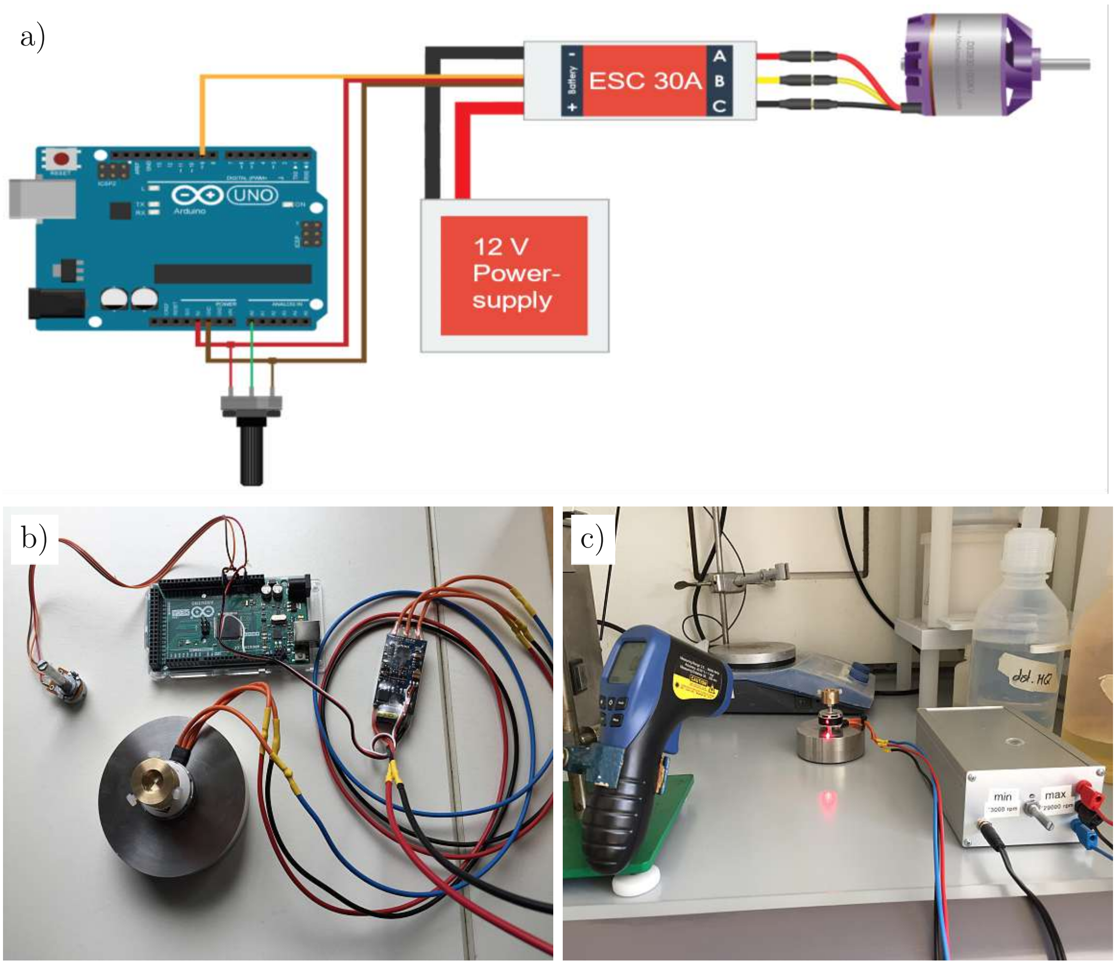

Figure 9: Spin-coater setup; a) circuit diagram, adapted from howtomechatronics.com [50] b) electronics without housing, c) fully assembled setup; laser spot from the tachometer and its reflection on the steel base can be seen in c).

The rotation speed of the motor was measured with a Tachometer PCE-DT 50, set to the desired value at the start using the potentiometer and then left constant during coating. A live measurement of the rotation speed was not performed to keep the splash shield in place around the motor when the solution is applied. The potentiometer-readings were observed to fluctuate $\sim \pm 100$ rpm and should be regarded within that accuracy, irrespective of the higher accuracy given by the manufacturer.

Due to the aforementioned excellent solubility of SEBS in cyclohexane [31], the coating made in this step can easily be removed and reapplied.

To quickly check the quality of the coatings before using the discs in SFA-experiments, the confocal microscope was used (see Section 3.4.3). Apart from discarding coatings with particles near the center that might interfere with the contact, the roughness parameters W_t, W_q, R_t and R_q were chosen as indicators for a satisfactory coating to proceed to the SFA-stage with a reasonable chance of a usable contact. Polymer coatings with $W_t \sim 400$ nm, $W_q \sim 100$ nm, $R_t \sim 100$ nm and $R_q \sim 25$ nm, or less were tried in the SFA (some roughness of the steel samples for reference in Section 3.4.3). The best coatings achieved with this setup in terms of roughness had $W_t \sim 160$ nm, $W_q \sim 40$ nm, $R_t \sim 80$ nm and $R_q \sim 7$ nm.

In order to determine the refractive index of the spin-coated SEBS layer – necessary for FECO evaluation – the refractive index was measured for a series of five cyclohexane-solutions with SEBS concentrations of 0-15 wt% and the results were extrapolated. The determined refractive index at standard pressure and temperature of ~ 1.52 is similar to the refractive index of polystyrene at 1.5894 and even closer to Poly(butadiene-co-styrene) (30% styrene) block copolymer – a precurser for SEBS at 1.5300 [51]. We are therefore very confident in the determined value. Details for the extrapolation are provided in appendix A.5.

3.3.3. SFA – Hardware

The SFA used was a home built SFA (see also Figure 3). In the optical setup several beam splitters, optical rail systems, irises, a 4× and microscope objective (Nikon), a LED cold white light source, a low-pass filter for wavelengths above 650 nm, an Andor EM-CCD sensor (338 iXon) and spectrometer (300 mm or 500 mm focal distance, 300 lines/mm up to 1800 lines/mm gratings with blaze angles around 550 nm) were used. [27] The effective resolution of these spectrometer/-camera combinations range from 0.02–0.04 nm. [27] The setup has been employed previously in published work in the group (for instance [27]) and continues to be optimized [52].

3.3.4. SFA – Software

A multitude of programs were used to control the SFA experiment. Their names, versions and respective purpose are listed in Table 3 below:

Evaluation of the FECO data uses a software named SFA explorer (version 3.5.1)

Table 3: Programs used to control the SFA, listing versions and main function.

Program	**Version**	**Function**
GSVmulti	1.39.6.7	Strain gauge measurements
ThorCam	3.5.1	Newton ring camera
Home-written code within LabVIEW 2018 [53]	18.0f2 (32-bit)	Piezo control
Solis	4.31.30022.0	FECO, spectrometer

that was coded in the group [27], see Section 3.3.6.1.

Forces acting on the strain gauge, recorded in mV/V are converted into mN by a python script when processing the data (see Section 4.2.1), based on a calibration of the strain gauge performed with five known weights. Details for the calibration are provided in appendix A.6

3.3.5. Sample Preparation

Optical discs, with a reflective Ti/Au coating already deposited in the PVD, were spin-coated with SEBS block co-polymer using a 9wt% solution in cyclohexane at ~3000 rpm. Specifically, 4-6 drops of solution were applied to the disc, rotating at a constant speed, at a ~2 s interval using a Pasteur pipette. After initial screening of the parameters rotation speed (3000-7500rpm), concentration of polymer solution (6-21wt% in 3% steps, the higher end of this range already proving too viscous) and droplet count (1-6), these conditions were found to produce acceptable coatings most consistently. Time-spacing of applied drops was initially not considered but leaving a small interval between drops was found to positively affect the resulting coating. To reduce the number of failures due to particles on the coating, the cyclohexane solution was filtered after preparation using a 0.2μm polypropylene membrane syringe filter (VWR International) and stored in a closed glass vial between uses. This filtering step increased the number of usable coatings significantly and is therefore regarded as critical.

Due to numerous error sources in the coating process (too many drops applied accidentally, drops not applied perfectly centrally, air bubbles, particles, damages to the coating while handling the discs,...) and the significant time the SFA-experiments take up, the coatings were almost exclusively prepared at least one day in advance to allow for multiple retries until the sufficient quality is met.

The coatings were then stored in a closed Petri-dish in the clean-room where the experiment was set. The sample set of steels characterized with SFA is the same as the contact-angle set (see Table 2): five thermally oxidized samples T1-T5, four plasma-samples P2-P5 and one reference sample REF, untreated, with its naturally formed oxide layer, each cleaned in ethanol in an ultrasonic bath and dried with a nitrogen gun before experiments.

In the SFA experiment, a suitable particle free contact was established between the polymer and the steel sample. The two surfaces were then separated ~400 mV in terms of the regulating piezo-electric crystal. Following this, a triangular signal was applied with an amplitude of 400 mV and a Frequency of 10 mHz, resulting in a constant approach velocity for all runs, periodically contacting the sample and then separating the surfaces. Three repeat cycles were done per sample as well as a repeat measurement on another platelet of the same steel.

3.3.6. Data Recording and Processing

The following data was recorded in each experiment:

- FECO (2.1.3.1) data from the spectrometer, recorded at a rate of one image per 0.1 s
- Force data from the strain gauge, recorded as mV/V at a matching rate of 1 data point every 0.1 s
- Newton ring data from the bottom view camera, recorded as static pictures taken at the instance of maximum compression

3.3.6.1. FECO Evaluation – SFA Explorer Briefly, FECO-analysis was exclusively performed with the software SFA-explorer (version 3.5.1), coded in the Applied Interface Physics group at TU Wien [27]. Simplified, SFA-explorer is used to fit simulated spectra to the measured spectra at a specific point in space (a horizontal line through the apexes of the FECO), minimizing the root mean squared deviation of the intensity profiles. This is done automatically by the software through systematic variation of estimated parameters (thickness of polymer coating, separation distance[2]), in a framework of fixed parameters (refractive indices of

---

[2] Starting at the point of maximum compression as a reference point, we know the separation distance there to be zero, so in that sense the parameter is not really estimated. However, we need to initially estimate which FECO-image captures this point of maximum compression, as

materials, thickness of semi-reflective layer, range of wavelengths passing through the filter), provided by the user. Once an initial image is fitted, the software can then fit an entire series of several hundred images, tweaking the fit slightly from image to image, adjusting polymer thickness in the compression/stretch phase and separation distance out of contact. Iterative improvements to the estimated starting conditions lead to a satisfactory fit across an entire contact-separation cycle, allowing us to link the measured forces to the separation distance of the surfaces in time.

3.3.6.2. Force Evaluation

The strain gauge data is processed by a python script [54], performing the following tasks:

- Organizing and plotting data
- Converting units (mV/V to mN)
- Fitting a baseline
- Normalizing by geometrical parameter (=optical disc radius; mN to mN/m)

The processed data then gives the force, normalized to the radius of the optical disc in mN/m dependent on the experiment time in seconds – a force-time graph, such as the example shown in figure 10.

This force time function was then matched to the distance information obtained from the analysis of the FECO (previous Section 3.3.6.1, using the characteristic behavior at jump-in, maximum compression and release for alignment. This step is necessary to eliminate the time difference that results from clicking the "run-button" in two different program-windows on the same controlling PC – typically ~0.5 s. This allows us to make force-distance graphs, which are a great help in determining the typical behavior of the system (see results, Section 4.2.1).

---

this can be exactly determined only after a series of images over a full contact-separation cycle is fitted, to which fitting a single image is the first step.

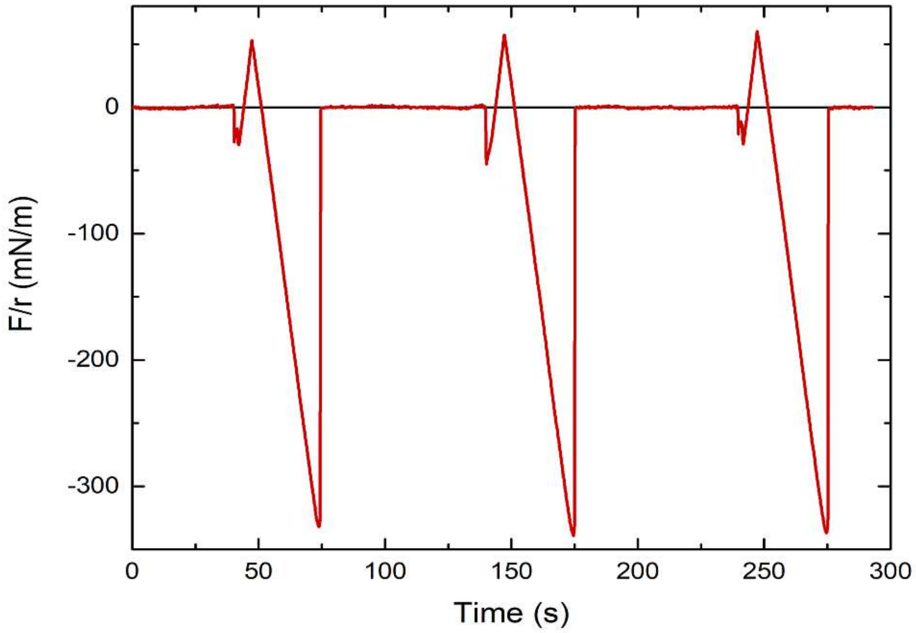

Figure 10: Typical force-time curve with three repeat cycles. Deviations from the zero-force line in order (left to right): adhesive jump-in, compression, adhesion.

3.3.6.3. Newton Ring Evaluation From the Newton ring images the projection of the real contact area was obtained by approximating the outline with a polygonal chain in ImageJ, as shown in Figure 11. This area can then – after a roughness correction – be used to convert the measured force into an adhesive pressure, an alternative to the Derjaguin approximation, as discussed in Section 2.1. Identifying the correct outline to follow is straightforward sometimes (panel a)->c)) and unclear in other cases (panel b)->d)).

It is helpful to carefully observe the behavior of the Newton rings during the experiment, but it is essential that repeat experiments are performed. In this case, if the one repeat experiment did not agree with the original one (or if no decision could be made), a third experiment was performed. In all cases this third experiment was in good agreement with one of the first two and the deviating one could be reconciled very well with the others by picking a different outline to follow. As the drawing of the polygonal chain had to be performed manually, this

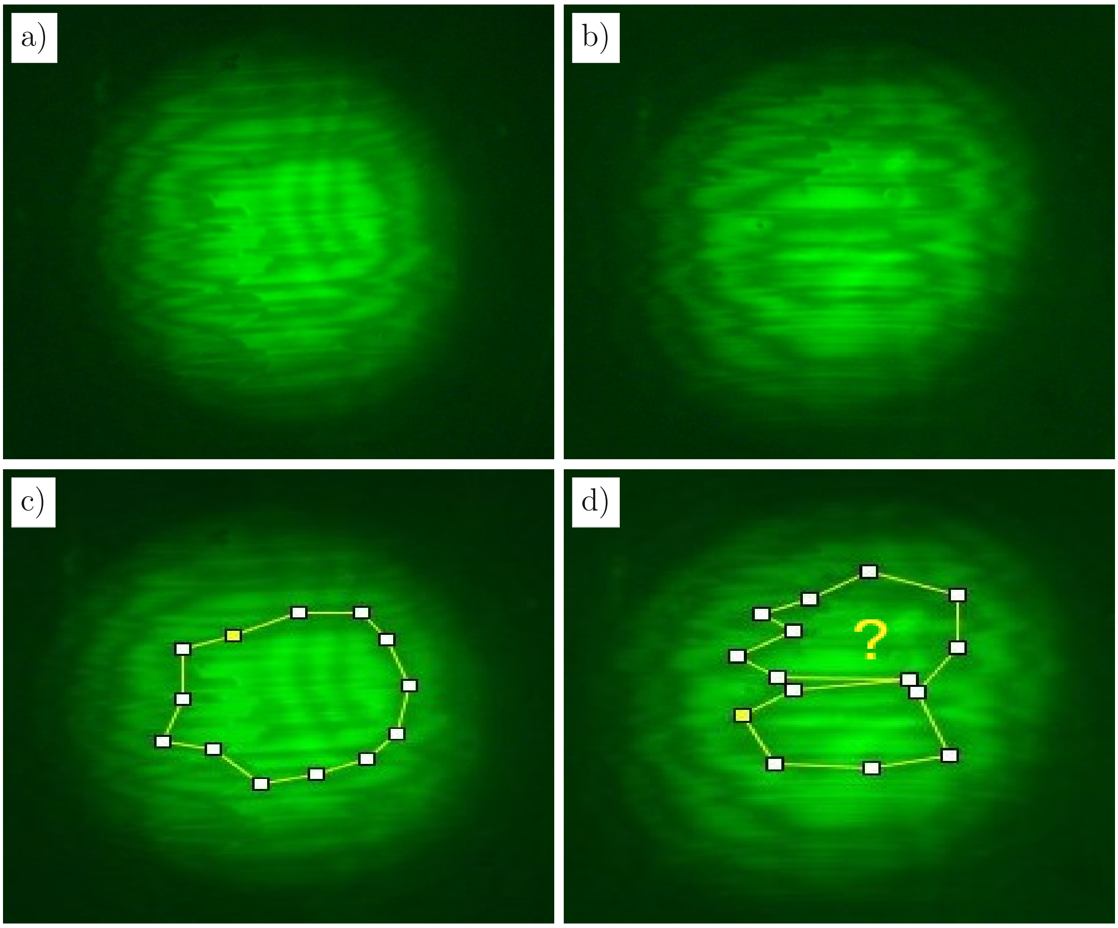

Figure 11: Polygonal fits to Newton ring areas; clearer case on the left, unclear case on the right.

step was repeated three times for each image. An average of the three resulting areas was then considered for normalizing the force to reduce the error introduced by manual fitting.

3.3.6.4. Roughness correction To achieve a roughness correction for the projected contact area obtained from the Newton rings, we have to make an assumption: The polymer, SEBS, is soft and elastic enough, to conform perfectly to the surface of the steel and establish full contact with no air-pockets in between. This assumption stands unproven in the context of this work, but we feel it is justified given the properties of SEBS discussed in literature (see Section 2.1.3.2) and also the fact that the results obtained from this experiment seem sensible. This problem was in fact anticipated from the start and the polymer chosen accordingly. But even with this assumption the true contact area cannot yet be calculated, as the precise location of where the steel was contacted and therefore the local roughness is unknown. A workable estimate was calculated from the global roughness as follows.

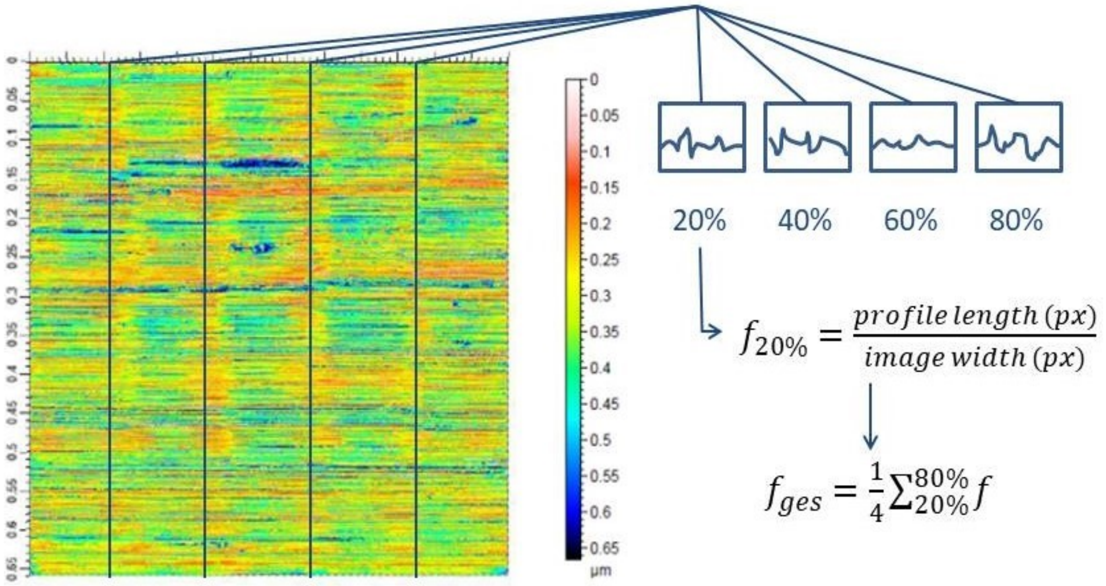

Figure 12: Schematic on how the roughness factor was calculated for each sample from confocal microscope pictures, averaging over four isolated line profiles perpendicular to the main direction of the roughness.

Since the roughness is highly directional, an approximation of the surface area can be obtained as shown in Figure 12, by multiplying the projected area by a roughness factor that only considers the roughness in one direction. This factor was obtained by extracting line profiles along the surface from the confocal microscope images and dividing the length of those profiles by the width of the steel sample. The roughness factor obtained by this method was averaged across four evenly distributed profiles for every sample. This approximation is flawed, its main drawback being that is does not give a handle on the local roughness, but it is good enough to make the repeat runs comparable. It has to be accepted for now that deviations in the local roughness add to the overall error of the technique.

The obtained roughness factor is then multiplied with the projected contact area obtained from the Newton rings to give a true contact area and the force measured in the experiment is normalized to this area instead of the geometrical factor (=the radius of the optical disc). A shift in unit from mN/m (an energy per area) to mN/m^2 (a pressure) is a consequence of this.

3.4. Corrosion and Repassivation Experiments

The goal of the corrosion and repassivation experiments was to develop a setup that enables studying repassivation in-situ when a scratch is applied and record an immediate system response in the form of changes in the element dissolution rates. In the following subsections we will discuss the electrochemical flow cell design, sample preparation and composition, as well as potential control and calibration for the ICP-MS.

3.4.1. Flow Cell

The electrochemical flow cell utilized in the experiments was self-designed, based on a previous design (Figure 13). The original design continues to be optimized in the group and has proven itself effective across numerous experiments [55,56]. The major difference here is the introduction of a rotatable teflon-seal directly above the working electrode (= the steel sample), which can be seen in Figure 14. A 0.5 (±0.1) mm glass bead is attached to the bottom of this seal, off center, by pressing it into the soft teflon until it sticks. When the seal is pressed against the working electrode during the experiment and rotated, it allows for scratching of the steel surface during the experiment, damaging the oxide layer and monitoring the repassivation behavior while repassivation is ongoing. Teflon was chosen as a material for both its softness, allowing for easy affixing of the glass bead without the use of glue, and, even more importantly, its low friction coefficient and self lubrication properties [57] , which allow even a tightly fit seal to be turned easily. Moreover it is also insulating. Electrode positions were not changed from the original design.

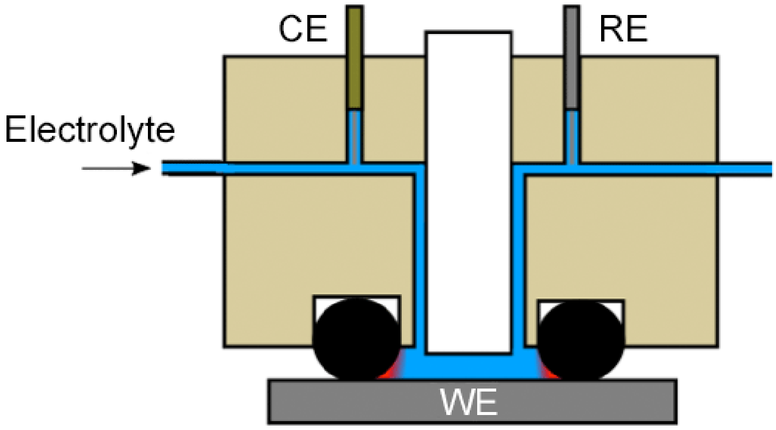

Figure 13: Electrochemical flow cell designed by Dominik Dworschak a former Ph.D. student in the working group of Prof. Valtiner. The electrolyte can flow from the left to the right reaching the ICP-MS after passing the counter electrode (CE), working electrode (WE) and reference electrode (RE) in that order. An O-ring (black cycle) prevents leaking of the electrolyte. Middle portion is glued in.

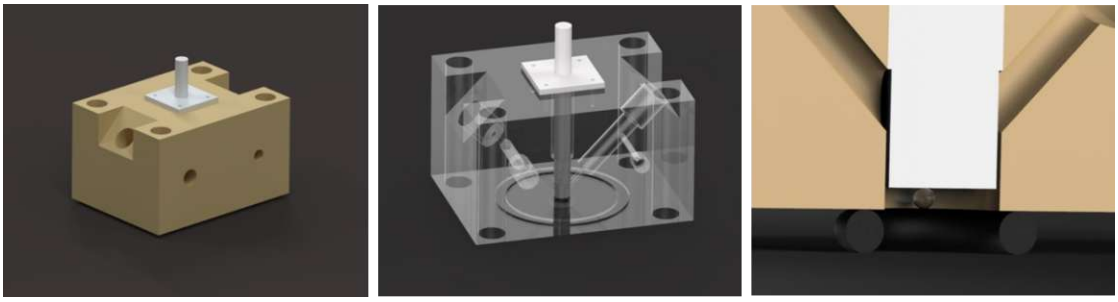

Figure 14: 3D-renderings of the scratching flow cell model; left to right: realistic, transparent material to show the channels, detail at the working electrode/scratching position

3.4.2. ICP-MS and Sample Preparation

All ICP-MS experiments were conducted on a 7900 ICP-MS from Agilent, coupled with a standard 3-electrode setup in the modified flow-cell, using a 1 mM NaCl solution as the electrolyte. Steel samples were prepared by sequentially grinding (with P400, P1000, P2500) and polishing (0.25, 0.1, 0.05 μm) for approximately 3-4 minutes at each grit and particle size. Prior to each measurement, the sample, flow cell and rotatable teflon seal were all cleaned in ethanol in the ultrasonic bath for 10 min. After each run, the seal, electrodes and flow cell were rinsed with water.

The full experimental setup is depicted in Figure 15. A standard three-electrode-setup is used to control and measure potentials in the cell. The peristaltic pump ensures a constant flow of the internal standard while the flow of the electrolyte, which is stored in the storage bottle, is manipulated by applying pressure with synthetic air.

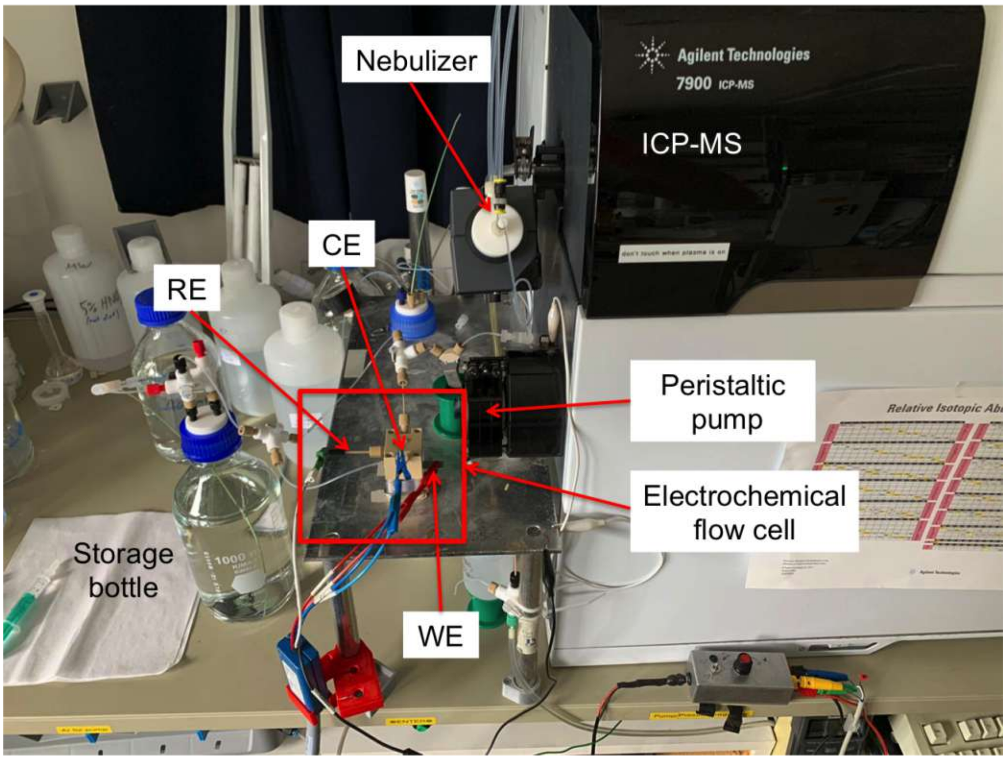

Figure 15: Electrochemical flow cell coupled to the ICP-MS; path of flow through the cell: IN (left) to OUT (back); counter-/working-/ and reference electrode labeled as CE, WE and RE respectively and passed by the electrolyte flow in that order (picture taken by Lukas Kalchgruber, figure used with permission from [58].

The flow of electrolyte through this system was controlled by monitoring the pressure from a ICP pressure sensor 1V2 (elveflow) at the exit of the flow cell, regulating to 80 mbar after the reservoir flask at the start of the experiment (software control via elveflow smart interface ESI 3.01.13). In successful experiments with no leakage, pressure only dropped briefly during the scratch itself, due to a blocked flow, and climbed up into a range of 70-80 mbar again immediately afterwards, remaining constant until the end of the experiment.

3.4.3. Confocal Microscope

The confocal microscope (μsoft explorer) was used in the SFA-experiments to determine the roughness of the steel samples (software μsoft metrology 7.4.4.13979). Individual roughness factors were calculated for each sample for evaluation as detailed in Section 3.3.6.4. Additionally, roughness parameters, both for the primary profile (P-parameters) and for the roughness profile (R-parameters), were determined by the analysis software μsoft analysis (version 6.2.6561). To differentiate roughness and waviness profiles a Gaussian Filter with 0.025mm cut-off was employed. Ranges for some parameters are given below; differences are not expected to correlate strongly with sample type, as all samples undergo the same polishing process before different oxidation processes, but the number of platelets cut out and analyzed in the microscope is insufficient to statistically prove this. The primary goal here was just to have a reference point. For details on roughness parameters see the norms DIN EN ISO 4287 and DIN EN 180 4287.

- P_t parallel to the groves 251-533 nm; perpendicular 360-557 nm
- P_q parallel to the groves 46-89 nm; perpendicular 68-95 nm
- R_t parallel to the groves 160-455 nm; perpendicular 245-493 nm
- R_q parallel to the groves 19-39 nm; perpendicular 35-65 nm

The microscope was also employed for the ICP-MS experiments. The two main purposes were firstly, checking the polishing after the sample preparation to ensure there were no major scratches or other surface defects remaining, secondly, finding the scratch applied during the experiment afterwards and documenting it. For future evaluations, this adds the possibility of estimating the depth and size of the scratch, which could lead to calculations that are independent of the scratch itself.

3.4.4. Samples

A list of investigated samples and their chemical composition is given in Table 4.

A closer look at the numbers of the table reveals that the investigated elements

Table 4: Chemical surface compositions for all model samples (MATEC GmBH) and industrial samples (Berndorf Band) investigated with ICP-MS.

Sample name	**Type**	**Fe w%**	**Cr w%**	**Ni w%**	**Mo w%**	**Mn w%**
FeCr4	Model	96.0	4.0	—	—	—
FeCr12	Model	88.0	12.0	—	—	—
FeCr16	Model	84.0	16.0	—	—	—
FeCr17.5	Model	82.5	17.5	—	—	—
FeCr17.5Ni10Mo2Mn1	Model	69.5	17.5	10.0	2.0	1.0
B1	Industrial	68.1	17.0	11.5	2.2	1.2
B2	Industrial	68.7	16.7	11.2	2.1	1.3
G1	Industrial	69.5	16.8	11.1	2.0	0.7

listed do not add up perfectly to 100% for the industrial samples but leave a remainder of 0.35%, 0.58%, and 0.49% for B1, B2 and G1 respectively. This remainder is made up of small amounts of Si, C, W, Cu, P, S and possibly other elements. The composition of industrial samples, determined by surface analysis, was provided by Berndorf Band.

The samples listed here can be categorized into three groups: The model samples with just iron and chromium, the more complex model sample with a composition closer to the steel that is actually used in the bands and samples of band steel from Berndorf labelled 'industrial'. The model samples with just iron and chromium will be used to determine the influence of different chromium contents on the passivation and corrosion processes without the presence and influence of other metals. The more complex model sample will be used to have a comparison for the industrial samples.

3.4.5. Electrochemistry

In the first stage of testing the system and performing initial experiments, the electrochemistry was kept as simple as possible and the same for all experiments discussed in this thesis. In the interest of comparability, every measurement started with applying -1.3 V versus the reference electrode (Ag/AgCl) for 20 min to remove the oxide from the surface and get similar starting conditions, as Fe^0 is the stable species then (see Pourbaix diagram, Section 2.2.1). The rest of the experiment was performed at open circuit potential (= OCP), waiting long enough to allow the dissolution to stabilize before scratching. The potential was recorded throughout the experiment in the hope of detecting changes in the OCP after scratching, but no such change could be detected and any immediate change from the scratch itself is completely masked by the signal fluctuation caused by touching the cell when manually applying the scratch. The software employed for potential control was EC-Lab software V11.12 from Bio-Logic-Science Instruments.

3.4.6. Data Evaluation

ICP-MS data was initially recorded as counts per second (CPS) for each element selected, using Mass Hunter 4.3 Workstation software for 7900 ICP-MS (version C.01.03, Build 505.16, Patch 3) from Agilent Technologies. The measured data was then converted into the dissolution rate ν in units of, $\mathrm{ng\,s^{-1}cm^{-2}}$, with a calibration (background b, slope k) based on a standard series prepared from a multi-element standard (Inorganic Ventures, 3.1) and using a working electrode area A of $\sim 0.07\ \mathrm{cm}^2$. The following Table 5 gives slopes and backgrounds for the measured elements; graphs are provided in appendix B.1.

Table 5: Calibration results for ICP-MS.

Element	**slope**	**R²**
Fe	6780.30	0.998
Cr	17270.48	0.998
Ni	3461.88	0.996
Mo	4568.53	0.998
Mn	3964.92	0.998

$$\nu = \frac{(CPS - b)}{k} * \dot{m} * \frac{1}{A} \tag{14}$$

Additionally the data was corrected by the mass flow $\dot{m}$, calculated after collecting and weighing the waste (see Equation 14). The data was then further processed by applying a 5-point 50% percentile filter to eliminate most of the shot noise that severely impacts the original data. In this filtering method data points are replaced by the median value of surrounding points, making it an efficient option in removing shot noise in particular, according to originlab.com [59]. An un-smoothed graph can be found in appendix B.3 for reference.

4. Results and Discussion

Let us now see, how the three techniques introduced so far can provide us with useful information about the studied adhesion- and corrosion-systems, starting out with the most accessible technique: contact angle analysis.

4.1. Contact Angle Results

Like in the original experiment by Berndorf Band, water and diiodomethane were used as solvents, netting one point-cluster each at different polarities. For maximum comparability, the same method, the OWRK-method, was employed for evaluation as discussed in Section 2.1.2.2. Sample preparation was changed from the original experiment and each contact angle given for each sample is averaged over four recorded angles to counteract directional roughness as detailed in Section 3. For complete tables listing all of these averages that then go into the OWRK-plots, please refer to the appendix A.2. Table 6 just lists the averages over all the repeat experiments of one sample type, with the standard deviation, to give some indication of the uncertainty in the data.

Table 6: Averages (Av.) of contact angle results with standard deviations (S.D.) over each sample type for diiodmathane and water. Multiple water-sets for sample P2.

Sample Type	CH_2I_2 **Av.**	CH_2I_2 **S.D.**	H_2O **Av.**	H_2O **S.D.**
T1	13.7	1.4	53.9	0.8
T2	28.0	1.9	58.9	2.1
T3	19.4	1.0	53.4	1.9
T4	15.4	3.0	49.9	3.1
T5	15.0	1.9	50.3	2.3
P2 - 1	30.4	1.4	65.0	6.6
P2 - 2	-	-	59.6	5.8
P2 - 3	-	-	52.9	2.7
P3	28.2	1.5	59.3	1.8
P4	26.3	1.6	55.8	1.9
P5	28.6	1.9	60.3	2.7
REF	23.5	2.2	43.9	1.5

As can be appreciated from this data, the averages, largely, are in good agreement with each other – the exception being the indicated sample P2 in the water-set (discussed separately at the end of the section). This agreement however, with many of the values falling within the desirable ±2° error that can occur even in good conditions [60] is misleading, as the values are already averaged over four angles. Considering the extreme directional roughness that made the averaging necessary in the first place it is not surprising that the original data varies more. What is surprising is how severely it varies – up to 9° difference in left and right angles of the same water droplet. This can no longer be explained solely with the dependency on the direction of the optical axis, although it is probably still an effect of the sample roughness. When the variation was extreme, the averages did not agree with each other, or the droplet shape was clearly irregular (example provided in Figure 16), the whole set was repeated and the data of the outlier replaced with data of a droplet from the repeat-set provided that the whole repeat-set was in good agreement with the rest of the original set.

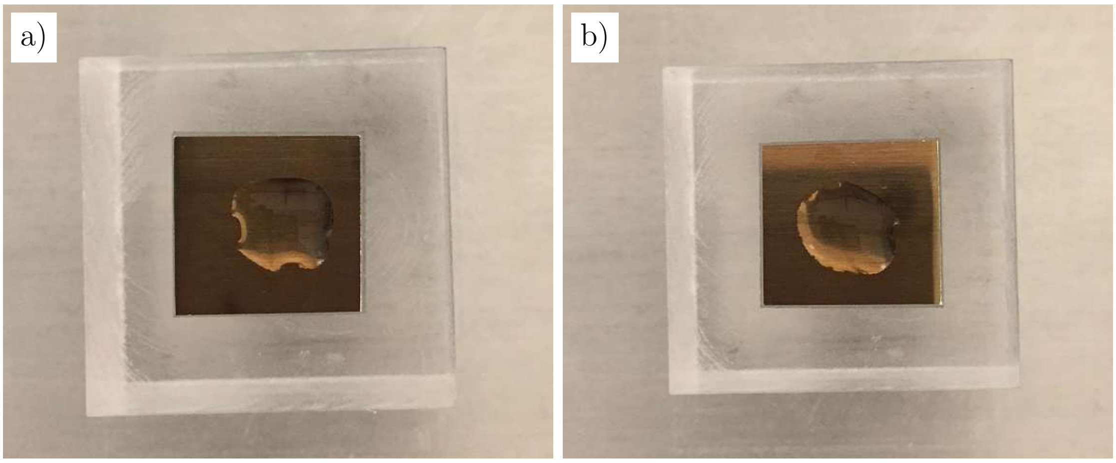

Figure 16: Irregular water droplets on samples from the T-series.

The averages were then plotted according to the OWRK-method as outlined in Section 2.1.2.2, giving two point clusters with varying y-values (see Figure 30 in appendix A.1). Following the original experiment performed by Berndorf, a linear correlation was assumed in accordance with theory. A linear regression was calculated and the polar and a-polar parts of the surface free energy obtained from its slope and intercept respectively (see OWRK-method, Section 2.1.2.2 and appendix A.1. This is problematic for several reasons – discussed later –, but was the chosen approach in the initial experiment.

Figure 17 depicts the experimental values for the total surface free energy, as well

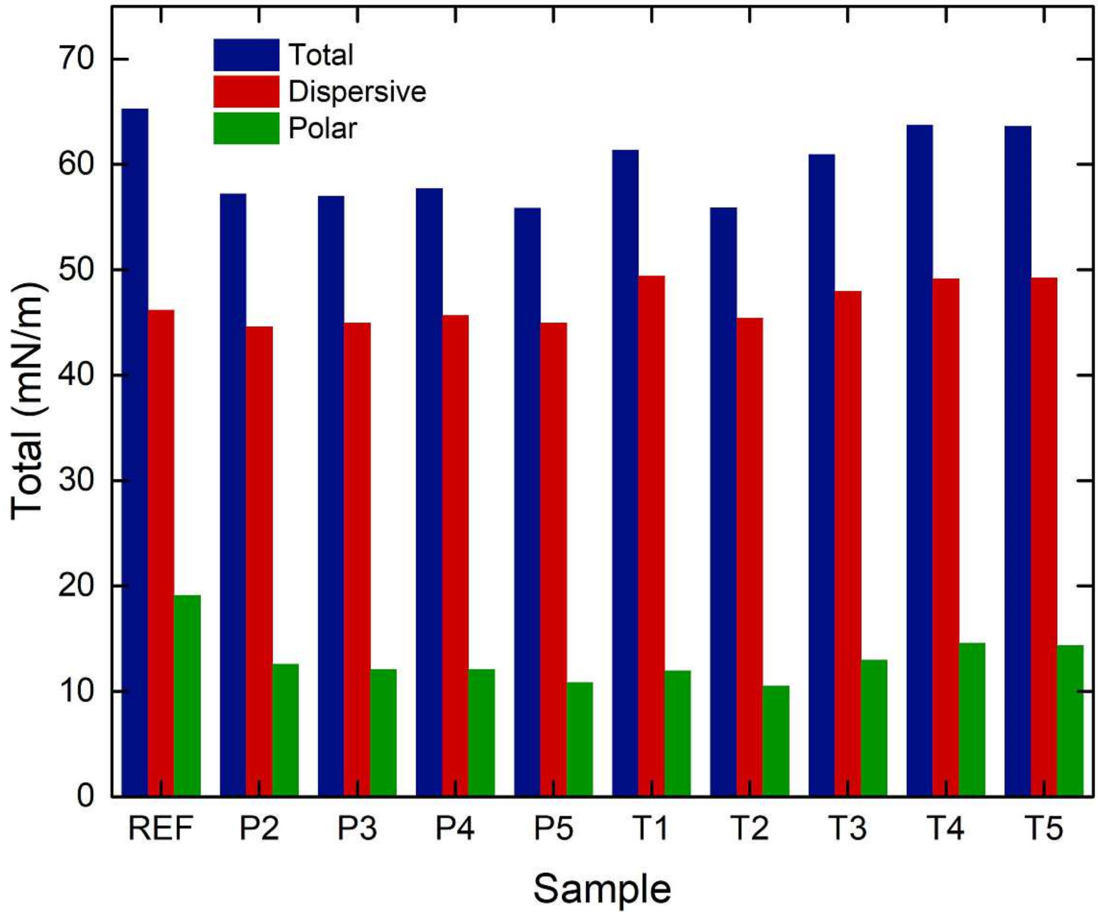

Figure 17: Surface free energy split into polar and dispersive parts from contact angle measurements for the untreated REF-, temperature-, and plasma-treated samples.

as its split into polar and dispersive components for each of the samples. The first thing to note is that the absolute values are strictly speaking not correct for the material, as no correction for the roughness was applied to adjust the angles. Theoretically the equation derived by Wenzel, Equation 5, would apply here, as discussed in Section 2.1.2.1, resulting in all the values being multiplied by a roughness factor r, which has to be determined for each sample. This was not done for a combination of reasons: Firstly, the absolute values are of little interest here, as they give no information about adhesive interactions with the steel, which was the property of interest, nor does it say anything about the differences between the different treatment-methods i.e. thermal/plasma oxidation. Secondly, as the base steel for all the samples is the same, the global roughness of these samples is very comparable; thus a shift in the absolute values should not occlude any trends. Finally, due to other error sources discussed adding to uncertainties in this data, we thought it better to concentrate time and resources on other methods, i.e. SFA.

The only conclusion that is safe to draw from these results, considering the quality of the data, is that the reference sample, titled REF, appears to have overall higher surface free energy than the oxidized samples. This is also what Berndorf concluded from their data. The rest of the data doesn't match unfortunately, possibly due to the differences in the experiments, and no trends within the oxidized samples are apparent in either data set.

Another point that needs to be addressed immediately about those results is the lack of error bars. The reason they are absent is that no meaningful error can be given using only two test solvents. Statistical reasons for this are discussed in appendix A.3.

This issue becomes immediately apparent when using a χ^2-approach instead of the least square fit to include the errors in individual points which are the errors of our averaged angles (see Section 3.2.3). It should be noted that the presented values for surface free energy in this experiment come from the χ^2-approach, as opposed to the original experiment by Berndorf, although there is negligible difference between the two fits. Table (7) lists the reduced χ^2_{red} for each sample in the water-set.

Table 7: Reduced χ^2_{red} for the linear model fits for all samples.

Sample Type	**Reduced χ^2_{red}**
T1	2.9
T2	12.0
T3	4.3
T4	6.3
T5	5.2
P2	30.5
P3	5.7
P4	11.5
P5	5.9
REF	16.7

The reduced χ^2_{red} in all cases are > 2, often much greater. This indicates that the linear model fits the measured data very poorly. Since the OWRK-method is not a postulate – we know the correlation to be linear – we can ignore this and use a linear model anyway, which is necessary to obtain any result at all from this data, albeit an unsatisfactory one. What we cannot do, is give any sort of error for these results, as the meaning of any error calculated from the linear model relies on that linear model actually describing the observed data well.

Another question that should be addressed is that of the, on first sight, significantly larger error for the water-set over the diiodomethane set, while a closer look at the data reveals significant variation in the contact angles for diiodomethane as well – especially percentage-wise. This can be understood when considering equation (6) used in the the OWRK-approach. As not the angle itself, but the cosine of the angle is considered, variations at smaller angles are suppressed, the cosine being very gently sloped there. Small angles with significant variation collapse almost perfectly into a single point in the diagram. Errors in the diidomethane-set therefore have very little impact on the resulting surface free energy.

Finally, to the exception of sample P2, all efforts to eliminate a trend towards smaller angles with repeated measurements on the same sample proved ineffective. Even though the additional drying step over phosphorus pentoxide eliminated the problem for all other samples, three measurements for the P2-sample still showed the trend 13. The reason for this behavior is not evident. To still include the sample in the overall result, the huge set of every repeat-measurement bundled together is considered, consisting of 72 total angles. The error on the resulting surface free energy, though not given, as it cannot be calculated from this data set for reasons already explained, can safely be assumed to be substantial. The result for the sample P2 should be viewed in this context and treated even more carefully than the other results of this experiment.

In brief summary: The results of this experiment are underwhelming and the comparability with the original experiment is, despite best efforts, very limited, if existent at all. The experiment design can be improved upon drastically:

1. Comparability suffers from the two different sample preparation methods (wet/dry). The long time the steel spent in lying around with a sticky foil on the surface is another error source.

2. Perhaps most importantly, two solvents are not enough, especially for calculating an error. Additional point clusters should make it much more likely that the statistical test for a linear model gives a good fit. A χ^2-method should then be used to calculate that fit to allow for error progression stemming from the averaging of the four different angles per droplet. It is not ideal to compare a χ^2-fit to a least-square-fit, but but may be acceptable, as

the fits give very similar results for all but the highest point errors.

3. It is problematic that in the original experiment, the influence of the directional roughness of the surface was not considered at all. Averaging over four angles is one way to attempt to solve this, as the surface roughness – unfortunately – is a given in this case and has to be worked around. Ideally both experiments to be compared should address this in some manner and agree in that manner.

4. The case of the sample P2 makes it apparent that the reason for a trend of lower and lower contact angles with repeat-measurements, which was believed to be residual moisture on the surface, may not be fully understood yet. Further optimization of sample preparation may serve to eliminate all such trends from the data and improve the apparent error.

5. Droplet size, a parameter that, because of the considerable and highly directional roughness, may have an influence on the error/reproducibility of the contact angle measurements was not explored in either experiment.

6. To get more accurate absolute values for the surface free energy and its components, the correction by Wenzel from Equation 5 should be used.

Whether it is worth it to optimize the experiment design like this, is up for debate. For now it remains questionable if a contact angle experiment can give reliable adhesion information about these samples. In the meantime we turn to a more direct approach to answer our questions: SFA.

4.2. SFA – Adhesion

4.2.1. SFA Results

Since the contact-angle approach yielded meager results and was plagued by inconsistencies – most likely due to the sample roughness – that could not be eliminated, we turn to another technique for more insight, SFA.

Before diving into the analysis of the FECO-data and the discussion of the results obtained from it, it is important to stress the range of quality in the data. Because of the – for SFA-purposes – significant roughness of the steel samples which is visible in the FECO data, as well as the fact that the FECO are necessarily recorded in reflection mode, resulting in less light-intensity being available, the quality of the recorded FECO varies greatly, as can be seen in Figure 18.

Figure 18: FECO data from different SFA-runs; a) control run against flat Au in transmission mode (FECO=white), b) better quality data (FECO=black), c) poor quality (FECO=black).

Figure 18 a) and b) are both of sufficient quality to evaluate sensibly, whereas c) is not. Not every otherwise usable contact has FECO of sufficient quality, due to limited light and local roughness, which makes pursuing full force-distance runs for all samples too time consuming. Therefore only one repeat cycle in a run for each of the sample groups, T-,P-, and REF-sample(s) was fully analyzed. Only simplified analysis of adhesive pressures was performed for all samples with a repeat for reproducibility.

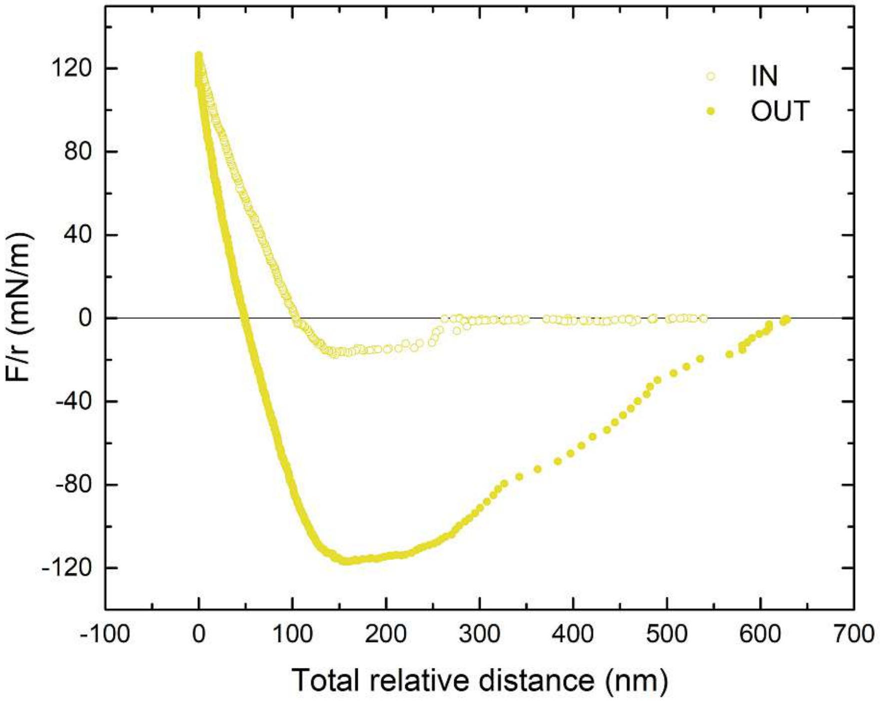

Figure 19: Force-distance curves for the reference run against flat gold, separated into IN- and OUT-run.

Let us start, however, with a brief discussion of the reference run against a flat gold sample, corresponding to the FECO in Figure 18 a). In the force-distance graph, Figure 19, we see the force drop below the zero-line in the IN-run, following the unfilled points from right to left, corresponding to attraction, but no jump in the distance. Following this we have a peak corresponding to compression of the polymer in contact, half in the IN-, half in the OUT-run, and a negative peak, corresponding to adhesion when we attempt to separate the surfaces. The adhesion phase stretches over a considerable distance, but this is not unexpected, as the elastic polymer stretches and is also considerably more rough than the smooth Au sample (roughness as PVD deposited). Where the measurement points begin to be more sparse in the OUT-run, we have the release, which again appears to be gradual, since we see no abrupt jumps on the distance axis between any two successive points that are more than a few nm.

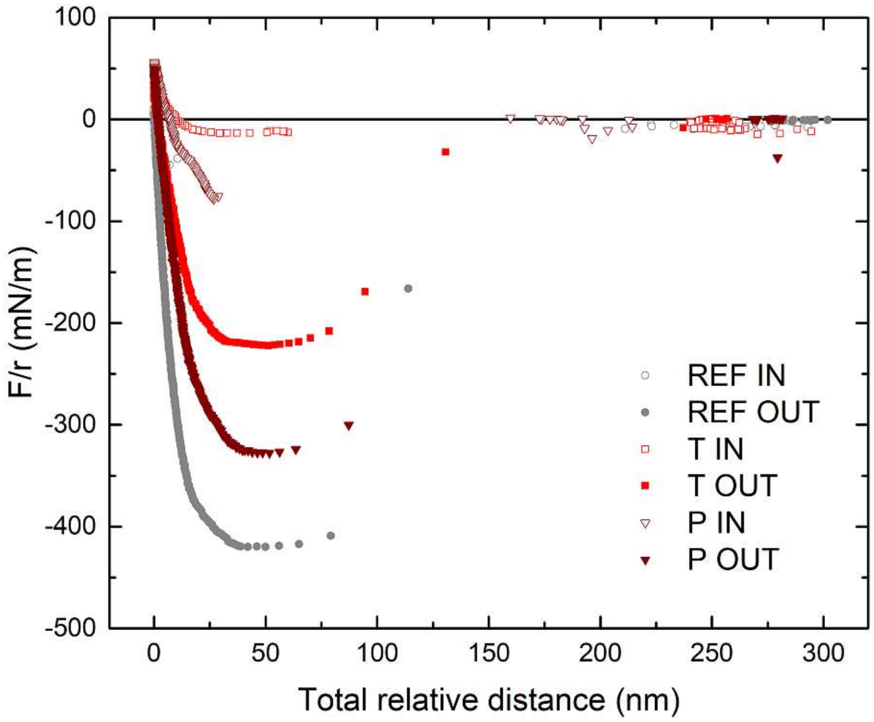

Figure 20: Force-distance curves for one example each of the P-, T- and REF-sample groups, separated into IN- and OUT-runs.

We can use this as a reference point and for comparison to the main experiment's data shown in Figure 20, an overlay of the resulting force-distance curves for the three different samples. The first feature of note in the IN-run, is an attractive jump into contact of ∼ 150 nm, accompanied by a dip in force below the zero-line (this abrupt change can already be seen in the force-time graphs, see Section 3.3.6.2, Figure 10). Unlike in the reference experiment against Au, the spring constant keeping the two surfaces separate is overwhelmed here. Following this, the polymer is compressed and the force spikes at a separation distance of zero. The compression occurs across a shorter distance than in the Au-run, but this is most likely due to fact that in the initial Au-experiment the polymer coatings were not yet optimized and may be of different roughness and thickness than the later ones. In the OUT-run, at first there is no separation but a strong adhesive force, followed by some stretching of the polymer up to a point (∼ 50 nm - 100 nm), where the contact breaks. This break is visible in the diagram as the force returning back to the zero-line within just a few measurement points that are hard to pin down with precision (due to the movement in the system reducing the quality of the FECO), and should therefore not be over-interpreted. In contrast to the Au-experiment, this is again an abrupt jump over a relatively large distance. This behavior matches the observations from the Newton rings exactly, where a flickering of the pattern can be observed during the experiment when the surfaces approach, which stops abruptly, when they jump into contact and restarts abruptly, when they separate. This also supports using Newton rings for a quicker evaluation of the adhesive pressure in the system. Overall, the shapes of the graphs in figures 19 and 20 are very similar, though attractive forces appear to be stronger in the case to the steel samples, leading to the noted differences.

Another thing worth noting from Figure 20 is that the trend we find in the end-result from most adhesive to least adhesive, REF>P>T, is already present at this stage, even though the adhesive force at this point is not yet normalized by the actual surface area, but by a geometrical constant (which, as argued in Section 2.1 is insufficient in this case) and the absolute values can therefore not be compared. This could be because large enough differences between sample types trivialize smaller differences in actual contact area, or it could be coincidental to some degree, since the FECO-data was only fitted for one sample each. Regardless, the actual contact area has to be determined to compare absolute values for the adhesion, requiring evaluation of the Newton ring data.

For the simplified analysis of the adhesive pressures the strain gauge data was processed as outlined in Section 3.3.6.2. The resulting force-time graphs (Figure 10 are reproducible in shape and show the same adhesion in repeat contacts within the same run (see appendix A.7). The adhesion appears not influenced significantly by contacting the same spot multiple times. Microscope images of the samples post-run also showed no signs of polymer residue or damage.

Across repeat runs, however, the values for the adhesion are not comparable. This is expected at this point and stresses again that the normalization of the force to the radius of the optical disc as geometric parameter (Derjaguin approximation; see Section 2.1), is not enough in this case, as the method depends on a smooth and rigid geometry and both the roughness of the steel sample as well as the elasticity of the polymer coating make these very bad assumptions in our case.

What we can do instead, is to correct for the projected contact area obtained from the Newton ring images rather than a geometrical factor, and additionally for the roughness of the steel, applying the methods discussed in sections 3.3.6.3 and 3.3.6.4.

The results are summed up in Table (8) and displayed in Figure 21.

Table 8: Adhesive pressures normalized by projected and actual surface areas and roughness factor for each sample type.

Sample	**Adhesive pressure normalized by projected surface area (mN/mm²)**	**Roughness factor f_r (1)**	**Adhesive pressure normalized by actual surface area (mN/mm²)**
T1	55.6	15.2 ± 2.0	4.2
T2	45.1	13.2 ± 2.8	4.0
T3	43.4	11.3 ± 1.1	2.9
T4	50.2	15.2 ± 0.9	3.0
T5	56.5	16.5 ± 1.2	4.6
P2	91.9	12.4 ± 2.1	6.3
P3	94.6	14.6 ± 1.1	5.1
P4	118.3	18.7 ± 3.2	6.1
P5	112.6	19.4 ± 2.1	6.7
REF	127.1	16.9 ± 3.1	8.4

The first thing to note before diving into discussion is, again, the lack of error bars for the individual measurements in Figure 21. The reason they are missing is simple: there is not enough data here to calculate a reliable error and estimating it from all the steps summed up is hardly feasible given the number of potential error

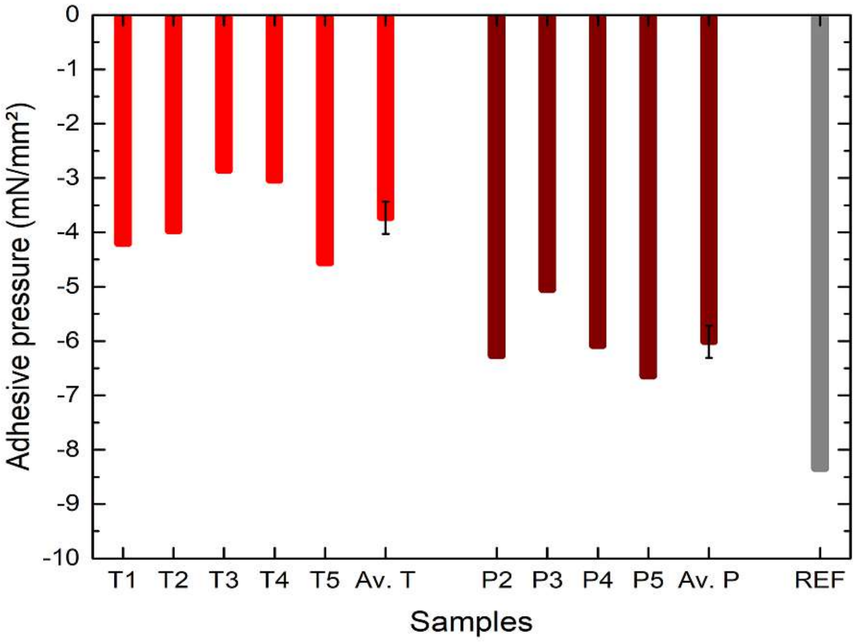

Figure 21: Adhesive pressures for all samples normalized by actual surface area (Av.= group average for sample group).

sources. Due to time constraints, only 2-3 repeat runs were performed to obtain an adhesive pressure for each sample type – at least twice would be desirable. But, although we cannot give error bars, we can give some numbers that allow a rough estimation of what the error might be. The largest deviation of repeat runs, for sample P3, is 17% ; the average is 10% , with half of the samples falling below that mark (taking the larger value as the base-value). Table (9) shows some differences between different samples compared to this average and maximum deviation for one sample.

This rough estimate does not replace calculating a standard error associated with the technique once the data is available. In the meantime though it is not without merit. For instance, we can be fairly confident that the technique can differentiate between the reference sample and the rest, but the adhesion-values for the highest T-sample (T5) and the lowest P-sample (P3) might be too close.

What we can differentiate for sure with this technique is an average T- from an

Table 9: Differences between sample groups. For comparison: average deviation of repeat experiments of the same sample was 10%, maximum was 17%

Samples	**Difference (%)**
REF-avg. T	55
REF-avg. P	28
Avg. T-avg. P	38
T5-P3	10
REF-P5	20

average P-sample, since we can calculate an error on these averages (from 5 and 4 values respectively). A two sample t-test assuming equal variances on these two sample sets gives a p-Value of 0.001 corresponding to a confidence level of >99%. The plasma treated samples on average show significantly more adhesion to the polymer than the thermally oxidized ones.

Moreover, since SFA was not the only technique used to study these samples, we have other information supporting this result. Firstly, the reference sample, REF, can also be differentiated in the contact angle experiment, showing a higher surface free energy. Secondly, it also is the sample type associated with most sticking-problems from Berndorf experience, matching the higher adhesive pressure found in the SFA-experiment. Thirdly, when considering functionality on the surface, analyzed by Lukas Kalchgruber with XPS at the Ceitec Nano Research Infrastructure, a correlation can be found with the percentage of -OH functionality on the surface as opposed to the oxide, shown in Figure 22. Testing the correlation coefficient on the basis of a two sided t-distribution gives a p-value of 0.004, allowing us to reject the null-hypothesis of an uncorrelated sample, again with a very high confidence level of >99%. As expected from the oxidation method, T- and P-samples have very different ratios of -OH functionality on the surface, which, as shown here, correlate to their adhesive behavior.

A hypothesis explaining this correlation is that although the influence on van der Waals forces 2.1.1.1 – the likely dominant interaction contributing to the measured adhesion – is not immediately apparent, the percentage of -OH functionality on the surface greatly impacts another possible attractive interaction: weak hydrogen bonding. The strongest possible H-bond in this system, the O-H $\cdots\pi$ bond, calculated for gas-phase dimers at ~ 2.8 kcal mol^{-1} [61], can only be formed if O-H functionalities are present on the surface of the steel. It is substantially stronger than the competing C-H $\cdots$O bond at $\sim 0.3 - 0.8$ kcal mol^{-1} [62–65] that forms

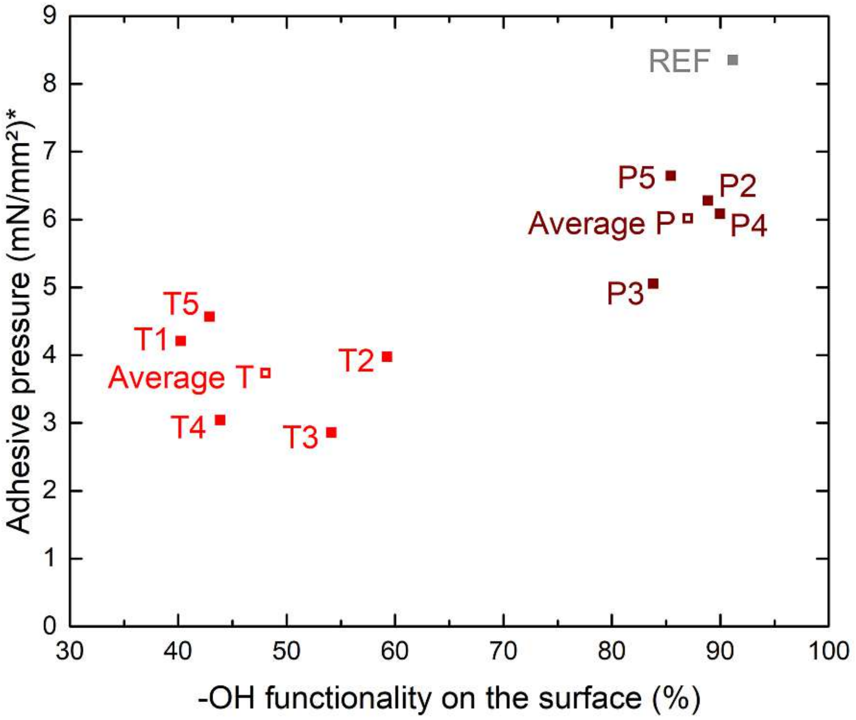

Figure 22: *Modulus of adhesive pressure ($|y|$) from SFA-experiments plotted against %-OH on the surface from XPS-data.

if there is no O-H available, resulting in higher adhesive pressure for samples with more O-H functionality at the surface (see also Section 2.1.1). Note that the referenced data stems from theoretical calculations and is meant only to allow a rough estimate, and some deviation in the practical case is expected. This nicely supports the difference between T- and P-samples found in the SFA experiment, but it is hard to quantify the impact of H-bonding on the overall adhesive behavior. Though the trend goes in the right direction, the hypothesis also very poorly explains why the reference sample has higher adhesive pressure, as the difference in % -OH to the P-samples is marginal. This is a good reminder that there are other factors at play as well, one of which is the thickness of the oxide layer. Since van der Waals interactions strongly depend on the density of the material, as discussed in Section 2.1.1, a thinner oxide layer, with much lower density than the metal, results in greater adhesion. Argon-sputtering experiments performed on the XPS by

Lukas Kalchgruber show that Fe^0-species are found at considerably smaller depths for the naturally formed oxide layer (REF$\sim 4-8$ nm), than for plasma-oxidized samples (P$\sim$ 50 nm), than for thermally oxidized samples (T$\sim>$ 100 nm). Practically this means a density difference between the samples well within the range of the van der Waals forces (compare adhesive jump-in at $\sim$ 150 nm), leading to differences in the contribution to the overall adhesion.

Taking into account the information from these additional experiments, we can feel more safe about our claim that the three sample types can be differentiated in terms of their adhesive behavior through SFA-adhesion measurements, though differentiating samples within the same set is not possible until the error of the technique for individual experiments has been nailed down. Final certainty however, requires additional data, specifically repeat experiments for the REF-sample to statistically ensure a significant difference with a good level of confidence. It is also safe to assume that the thickness of the oxide layer is a critical parameter when it comes to adhesion – and not just in corrosion protection, where it may be more typically considered.

4.3. Corrosion and Repassivation Results

In this second part we will discuss results from the electrochemical flow cell-ICP-MS experimental setup discussed in Section 3.4, starting with, and focusing on, the simpler and more well understood FeCr-model samples (see table 4 for sample list).

4.3.1. Iron-Chromium Model Samples

The first set of experiments to discuss is that of the model samples containing only iron and chromium: FeCr4, FeCr12, FeCr16 and FeCr17.5. As mentioned in Section 2.2.1 it is well known that a certain chromium content is beneficial to corrosion resistance and we can expect therefore to see some differences in repassivation behavior. Of these four samples, the three with $\geq 12\%$ chromium behaved very similarly, while the FeCr4 sample's behavior was wildly inconsistent with the others and the steel was not always able to repassivate. Figure 23 shows such a case. Note that the chromium dissolution curve is multiplied by a factor of 200 for illustration purposes.

As the behavior displayed in this experiment was not reproducible, it will be

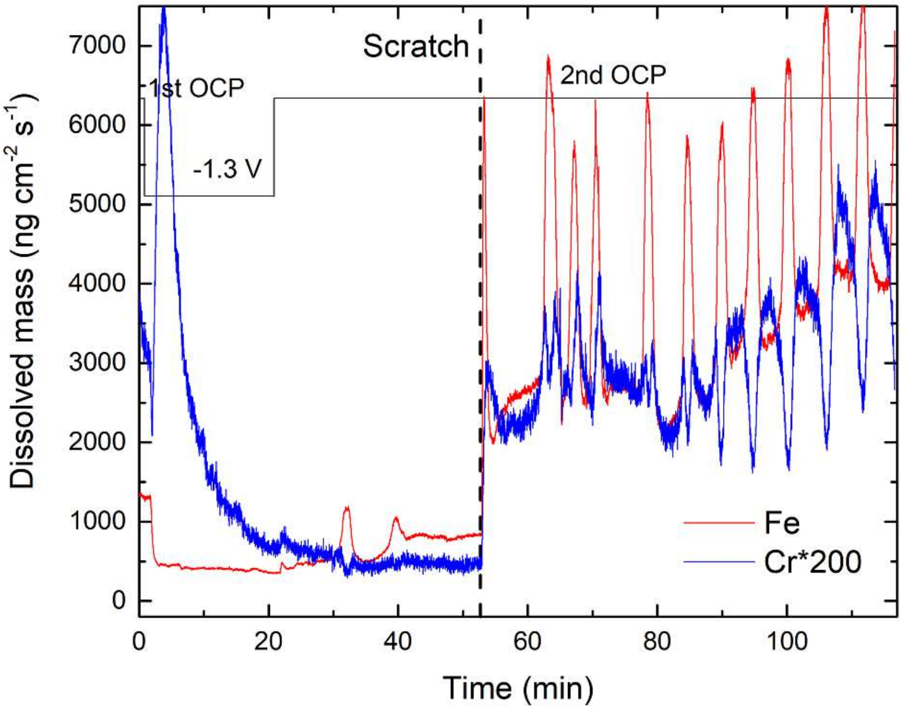

Figure 23: Sample FeCr4; mass flow of dissolved species normalized to the area of the working electrode; Cr dissolution curve scaled by a factor of 200.

discussed only briefly. The main feature of interest, we do not see with any of the other samples, is the periodic nature of the signal after the scratch. It appears that the sample cannot repassivate properly under those conditions due to the low chromium content. Other explanations, such as that we see an artifact in the signal, for example due to a blockage in the tubing, are highly unlikely, as we would see the dissolution of both elements spike at the same time and not the perfectly aligned dips in the chromium signal we observe for every spike in the iron dissolution. There is also the possibility that we observe a pitting corrosion phenomenon that is to some extent independent of the scratch, but more data would be required to confirm or rule out this possibility.

Graphs for the model samples with a chromium content of more than 4% are much more easily interpretable in comparison and do not show qualitative differences, unless there are artifacts present in the data, such as might be caused by the inconsistent nature of manual scratching, or a pressure drop due to a leak in the tubing. Figure 24 shows a typical scratching response for a repassivating FeCr-sample.

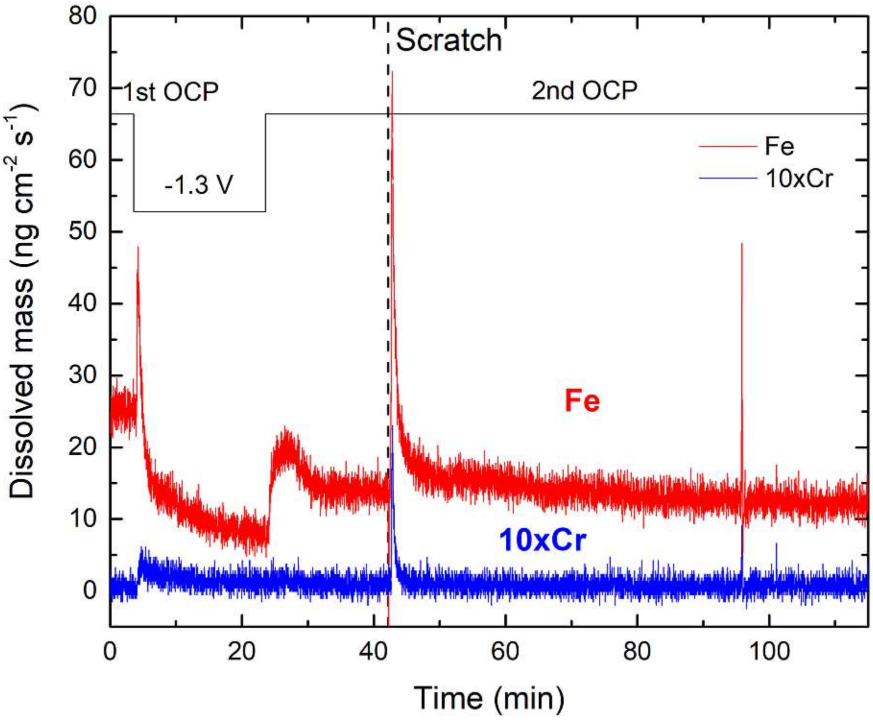

Figure 24: Sample FeCr17.5; mass flow of dissolved species normalized to the area of the working electrode; Cr dissolution curve scaled by a factor of 10.

Whenever the sample can repassivate, we observe a very similar response to the scratch as to the initial jump in potential from -1.3V to OCP. The signal decay appears to be exponential initially, but that model fits the data poorly if fitted up to the end of the experiment. Plotting the data logarithmically, we can obtain both a confirmation of this exponential behavior, as this section of the plot will appear linear, as well as determine an upper limit up to which to fit the exponential decay function (since this limit is not immediately apparent in figure 25 a)). Exponential fits of a form described by Equation 15a up to a limit determined individually for each experiment via the ln-plot (36-264s), describe the initial decay well with R^2 values >0.97. Figure 25 shows this fit for the FeCr17.5 sample in both plots. Again, no qualitative differences were observed between the higher chromium content model samples. Note that the considerable fluctuation of the signal in the later half of plot b) is mostly a byproduct of plotting the data logarithmically.

$$y(x) = y_0 * A_1 * e^{-\frac{x-x_0}{t_1}} \tag{15a}$$

$$\tau_{1/2} = \ln 2 * t_1 \tag{15b}$$

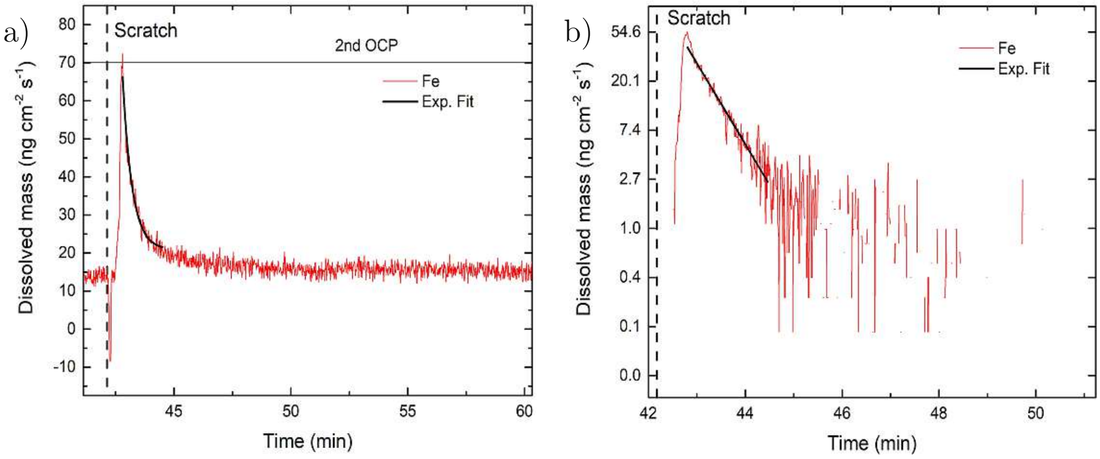

Figure 25: Iron dissolution after the scratch fitted with an exponential decay function in a) the original plot, b) the ln-plot for the sample FeCr17.5.

It is evident from these ln-plots that an exponential decay function will only describe well the time period immediately after the scratch. A better fit for the later part could be obtained using a linear model, but this brings its own problems, which we will briefly discuss in the summary and outlook Section 5, as they go beyond the scope of this thesis, as well as beyond what we can safely conclude from the available data. Focusing on the time immediately after the scratch we can ask whether the speed of the decay, which can be characterized by the half-life time from Equation 15b – which should correlate to the speed of repassivation – of the fitted exponential function, is characteristic of the measured sample and/or correlates in any way with the chromium content. The same half-life time calculations were also performed on the iron-dissolution profiles of the industrial samples. The recorded half-life times are given in Table 10.

The half-life times determined so far seem not reproducible and there is not enough data to determine the discrepancy. Observations during the experiments yield no

Table 10: Half-life times $\tau_{1/2}$ for model samples with varying chromium content and the industrial samples.

Sample	$\tau_{1/2}$ **Experiment 1 (s)**	$\tau_{1/2}$ **Experiment 2 (s)**
FeCr12	6.1	-
FeCr16	54.9	-
FeCr17.5	16.9	13
B1	17	15.2
B2	18.3	-
G1	78.6	22.1

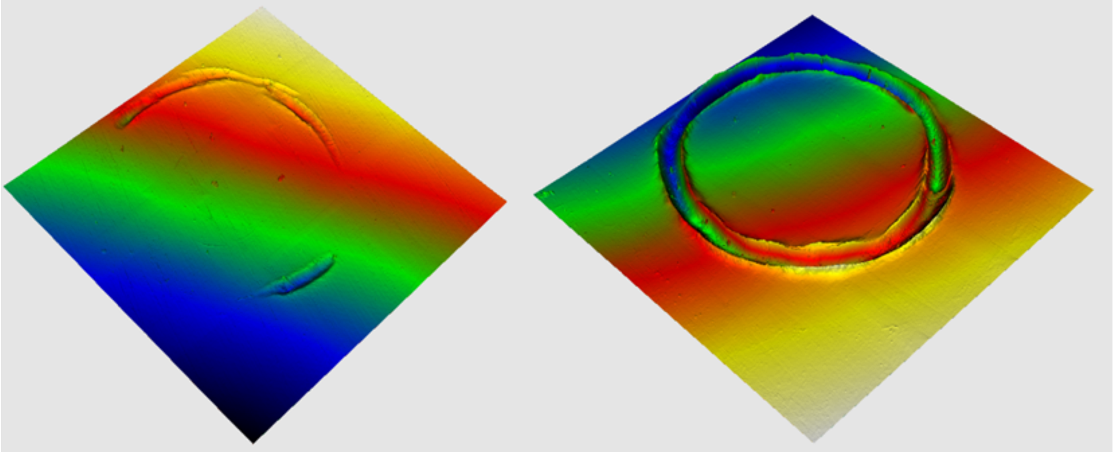

Figure 26: Visible difference in surface damage from scratching in different runs; sample B2 (l.) shows a not consistent scratch while FeCr12 (r.) shows a deeper and more consistent scratch; viewed section is $\sim 2.1 \times 2.1$ mm.

obvious explanation for large deviations such as in the G1 case. Furthermore, we cannot ascertain any trends with regards to the sample composition, where we would expect a correlation with the speed of repassivation. It is possible that repeats of these experiments show such a correlation, but no less likely than other influencing factors – that we did not control so far – dominating. A candidate for such a factor would be the the manually induced scratch: depth and area vary wildly from run to run, as can be seen in the post-experiment confocal microscope images in Figure 26. Another factor might be the OCP duration prior to the scratch, where oxidized forms of iron and chromium are stable (see Pourbaix diagram 4 in Section 2.2.1). It is hard to gauge during the experiment when the dissolution has stabilized; for future experiments a longer relaxation period before scratching may be desirable to make sure the dissolution is stable in all cases.

4.3.2. Dissolution Ratios

Another thing to look at is the ratio of dissolved species immediately after the scratch. Due to the inconsistency of manual sample preparation and scratching and the fact that the calibration was only done once, we are unable to quantify absolute dissolutions. However, we can expect the *ratio* of dissolved species to maybe be independent of this. To study this, the ICP-MS data is plotted in element-ratio plots where for each element its percentage of the dissolved species is divided by its percentage in the makeup of the sample. This way, if in the FeCr17.5 sample 17.5% of dissolved species were chromium, the line for chromium would appear at the marked value of 1. The actual data for the sample FeCr17.5 is displayed in Figure 27; graphs for FeCr12 and FeCr16 show the same features.

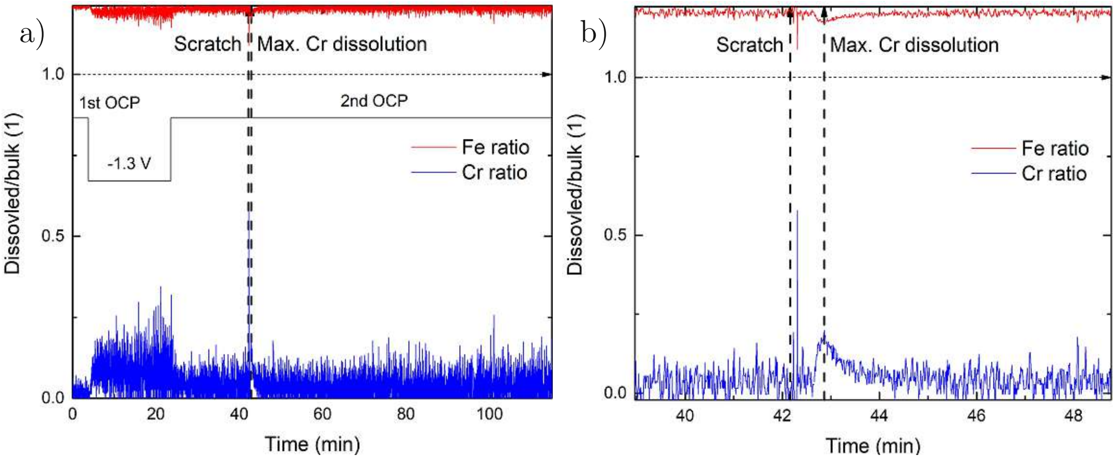

Figure 27: Sample FeCr17.5 dissolution ration plots; whole plot a) and section of interest at the time of the scratch b).

These graphs show that we indeed observe a preferential dissolution of iron over chromium that persists through the whole experiment, regardless of the scratch. Chromium species never account for more than ∼ 5% of dissolved species in all cases, despite making up 12-17.5% of the sample´s surface, depending on the sample. We observe that the share of chromium dissolution was slightly higher when a negative potential was applied and lower when the sample was kept at OCP. Zooming in on the scratching time we also find another consistent feature otherwise hidden in the noise. Immediately after the scratch two things happen in the plot:

1. The fluctuation lessens (due to the spike in absolute dissolution)
2. The share of chromium dissolution rises briefly while the share of iron dissolution dips.

With the second point it is not immediately apparent why this should be the case, but one possible explanation is to assume the peak to be primarily or exclusively material being removed by the scratch, as the surface oxide has a higher Cr-content. This would mean, however, that $\tau_{1/2}$ is not characteristic for the repassivation speed - as is the hope so far.

4.3.3. Multi-Element Samples

The results for the more complex multi-element model sample and the similarly composed industrial samples are unfortunately much harder to interpret. The iron dissolution curves can be viewed independently and subjected to the same half-life time analysis we employed for the FeCr-model samples (results have already been shown in Table 10).

There are a few observations we can make from the dissolution plots, Figure 28:

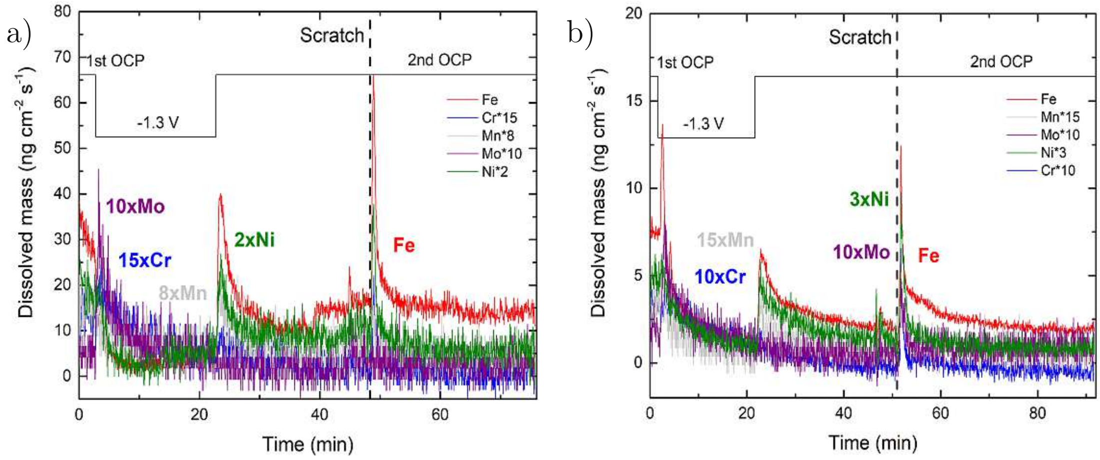

Figure 28: Repeat experiments on the industrial sample B1; dissolution curves for different elements scaled as indicated for illustration purposes.

- Mo and Mn do not react to the scratching consistently in any way we can measure
- Ni-dissolution spikes both with a potential jump as well as when the sample is scratched
- Mo dissolution spikes when a negative potential is first applied, decaying over time (this is observable in all experiments, though not equally)

The last of these observations is consistent with other experiments done in the research group and hypothesised to be the result of molybdenum oxides, previously formed on the surface, dissolving. Molybdenum oxides are known to form on molybdenum surface-enriched steels and impact corrosion behavior positively [44].

Unfortunately, the element ratio plots become largely uninterpretable, due to large fluctuations which get worse the more elements – especially with relatively small surface concentrations – are plotted. An example is shown in appendix B.4 for reference.

Before drawing further reaching conclusions, some improvements to the experiment setup may be necessary – suggestions are given in the outlook Section 5.3 – and more data will have to be gathered. I would like to close the discussion section with an example showing why it is so difficult to draw definitive conclusions from the limited amount of data gathered so far. Figure 29 shows an experiment on the sample B2 – almost identical in composition to the just discussed B1 (compare Table 4), yet showing several anomalies.

- The Mo-dissolution spike when switching to -1.3V is much more pronounced than in any other experiment
- Mn-dissolution spikes at the return to OCP, which we do not observe in other experiments
- Fe dissolution drops inexplicably shortly before the scratch
- Two unexplained spikes in Ni-dissolution in the -1.3V regime

Reasons for inconsistent behavior occurring in some of the runs are hard to pin down but may include inhomogeneities in the oxide layer or differences in the sample preparation (polishing). Previous electrochemical steps, like the duration of the OCP prior to scratching, or the -1.3V step are another possible influence. More experiments are required to determine which of these parameters are critical.

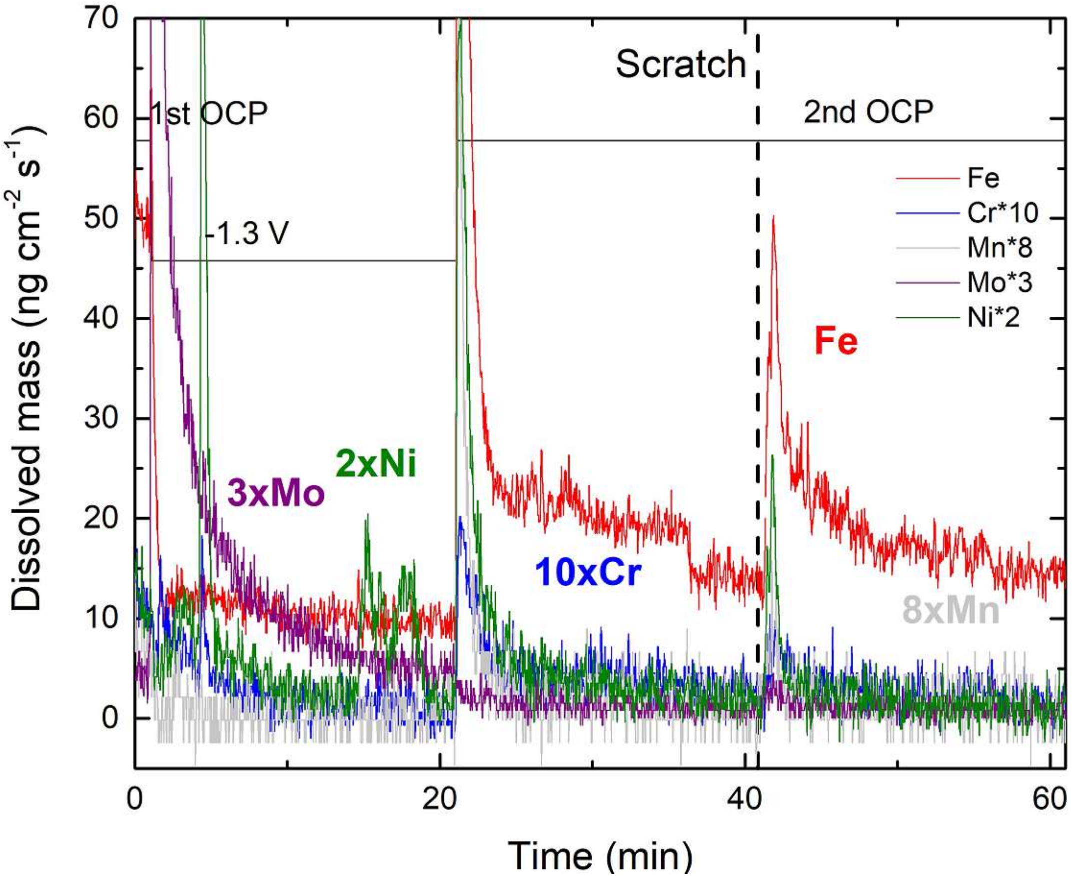

Figure 29: Dissolution curves for sample B2; dissolution curves for different elements scaled as indicated for illustration purposes.

5. Summary and Outlook

5.1. Contact Angle

In the light of the SFA results the contact angle approach holds little more promise. The main result of the experiment, the difference between the reference sample and the oxidized samples, is supported by the SFA, and is also quantifiable. The difference between the P- and T-samples, showing some dependency on the ratio of oxide to hydroxide functionality, is potentially very hard to pick up on even in an ideal contact angle experiment. The reason for this is that there is no apparent reason H-bonds from water to either surface functionality should be preferred energetically by a considerable margin. Moreover, the highly directional roughness of the steel samples also makes the approach ill-suited to the problem at hand. The experiment can definitely be optimized to better answer the research questions and give more robust results, but the time investment is hard to justify over more promising techniques such as SFA.

5.2. SFA

The SFA results presented in this thesis are more promising, albeit incomplete. Considering the additional information presented that we have from other experiments, we can feel fairly confident in the assumption that we have a method at our hands – in SFA with complementary XPS – that allows us to quantify the adhesive pressure in a model system and differentiate between differently treated steel samples. Additional information, such as information on the oxide layer thickness, will have to be gathered to asses presented hypotheses and more confidently determine why this difference is present. The insight this approach gives into the problem is a nice first step in the right direction, but there is more work to be done. Above all, repeat experiments have to be performed to determine the uncertainty in the technique and enable discussion of improvements. As an example: the method of approximating the local surface roughness is rather crude at the moment, but it is impossible to say how much it impacts the overall error, as that is as of yet unknown.

The main selling points of the technique are as follows: Firstly, the model system is very close to the actual problem, as the steel sample in question can be used directly. Secondly, direct information about the adhesive pressure can be obtained, as opposed to the contact angle approach. Thirdly, much more additional information about the adhesive behavior of the system is available beyond just one number.

The main drawbacks are: Firstly, how time-consuming the experiments are. This drawback is more prominent in the beginning, when the technique is still being developed and it is likely that the experiments can be drastically sped up. Especially in the sample preparation steps (spin-coating) and in evaluation (initially very hard for such rough samples) a lot of time can be saved. The SFA-part itself however will remain a somewhat time consuming experiment. Secondly, while the steel side of the experiment is rather flexible and the samples of interest can be directly used in the SFA-experiment, so long as they are reflective enough, the polymer side is more limited. Finding an alternative to SEBS is definitely possible, but the property requirements for the full adhesive contact despite the rough surface, as well as the requirements for spin-coating, limit the possibilities drastically. Thirdly, while the adhesive pressure can be quantified and compared within the model system, a comparison to other adhesion data sets in literature remains problematic. The reason for this is not just a difference in units (adhesive energy/adhesive pressure, see Section 2.1), although no convenient conversion factor exists, but also a problem inherent in the experiment itself – the polymer deformation. This elastic deformation (stretching) contributes to the measured adhesive pressure and is not easily factored out. Comparisons with results obtained from other experiments, where this elasticity is not present should therefore be treated with care.

5.3. Corrosion and Passivation

Important first steps were taken to attempt to study repassivation of steel samples in-situ after damaging the oxide layer, but there is a lot of work yet to be done. Design and proof of principle for a scratching cell were completed and initial experiments performed on a variety of samples. The main takeaways so far are optimization potential for future experiments and models developed to evaluate the data. One of the main challenges will be learning which experimental parameters have to be controlled and how tightly to achieve better reproducibility. Many repeat experiments, preferably for the simpler model sample initially, will be necessary to establish this before a much wider space of experimental parameters, such as different electrolytes and concentrations or applied potentials, can be explored. Repeat experiments will also show whether the, so far irreproducible, half-life time turns out to be the characteristic parameter we hope it is, or whether the inconsistency of the manually applied scratch has an influence on it. Lessons learned so far to improve future experiment design include:

- Longer run-times after scratching to better study a potential linear decay after the exponential one to determine the passive dissolution.
- Additionally longer stabilisation time before the scratch and time before the negative potential is applied to allow the determination of if and when a base level of dissolution is reached again after the scratch.
- More consistent scratching (automation) might be necessary for consistent results.

On the data evaluation side a good alternative for the element-ratio plots that works for the more complex industrial samples would be desirable. Aside from that, more data will have to show whether or not half-life times for industrial samples (calculated purely from the iron dissolution curves) are directly comparable to the half-life times for the FeCr model samples, considering the amount of nickel dissolution when scratching. We cannot be sure about a possible linear decay following the exponential one from the data presented in this thesis; on the one hand, because some experiments were stopped too early, on the other hand, because some of the slopes for the fits of these parts are close to zero and should not be considered strong support for the model. Recent follow-up experiments performed in the group, however, would suggest that the application of a linear model for the passive dissolution is justified. From a brief look at the available data so far, we can already conclude that applying both an exponential and a linear fit to the data will leave an unfitted transition period that might need more complex mathematical models – another challenge for future evaluation.

Finally, it will have to be evaluated whether automation of the scratching will be necessary to move forward with this type of experiment. If so, a cell design developed with this in mind should serve as a good starting point.

5.4. Overall Conclusion

In the course of this thesis, analytical tools and methods were developed and adapted to deal with questions about corrosion and adhesion properties of steels. Of these, the SFA-approach to measuring adhesion is quite far progressed showing a correlated trend with XPS data; the ICP-MS scratching experiments, albeit promising, are still in the early stages and need more time investment to optimize.

References

[1] `https://www.berndorfband-group.com/en/products/steel-belts/foil-and-film-industry/`. Accessed: 2022-08-29.

[2] J. Sun, H. Tang, C. Wang, Z. Han, and S. Li, “Effects of alloying elements and microstructure on stainless steel corrosion: A review,” *steel research international*, vol. 93, no. 5, p. 2100450, 2022.

[3] G. Sergi, “Ten-year results of galvanic sacrificial anodes in steel reinforced concrete,” *Materials and Corrosion*, vol. 62, no. 2, pp. 98–104, 2011.

[4] N. Stavlid, *On the Formation of Low-Friction Tribofilms in Me-DLC – Steel Sliding Contacts*. PhD thesis, Uppsala University, Department of Engineering Sciences, 2006.

[5] Y. Yan, P. Zhou, O. Gharbi, Z. Zeng, X. Chen, P. Volovitch, K. Ogle, and N. Birbilis, “Investigating ion release using inline icp during in situ scratch testing of an mg-li(-al-y-zr) alloy,” *Electrochemistry Communications*, vol. 99, pp. 46–50, 2019.

[6] Y. Xie, J. J. Jiang, and M. A. Islam, “Applications of elastomers in slurry transport,” *Wear*, vol. 477, p. 203773, 2021. 23rd International Conference on Wear of Materials.

[7] P. Ponthiaux, F. Wenger, D. Drees, and J. Celis, “Electrochemical techniques for studying tribocorrosion processes,” *Wear*, vol. 256, no. 5, pp. 459–468, 2004. Special Issue on Tribo-corrosion.

[8] C. Bandl, W. Kern, N. Krempl, and W. Friesenbichler, “Simple and rapid method for restoring anti-adhesive organosilane coatings on metal substrates,” *Progress in Organic Coatings*, vol. 140, p. 105490, 2020.

[9] B. Kaynak, C. Alpan, M. Kratzer, C. Ganser, C. Teichert, and W. Kern, “Anti-adhesive layers on stainless steel using thermally stable dipodal perfluoroalkyl silanes,” *Applied Surface Science*, vol. 416, pp. 824–833, 2017.

[10] R. J. Good, “Contact angle, wetting, and adhesion: a critical review,” *Journal of Adhesion Science and Technology*, vol. 6, no. 12, pp. 1269–1302, 1992.

[11] J. N. Israelachvili, *Intermolecular and Surface Forces*. Academic Press, 3 ed., 2011.

[12] T. Steiner, "The hydrogen bond in the solid state.," *Angewandte Chemie*, vol. 41 1, pp. 49–76, 2002.

[13] P. Roura and J. Fort, "Local thermodynamic derivation of young's equation," *Journal of Colloid and Interface Science*, vol. 272, no. 2, pp. 420–429, 2004.

[14] J. Wang, Y. Wu, Y. Cao, G. Li, and Y. Liao, "Influence of surface roughness on contact angle hysteresis and spreading work," *Colloid and Polymer Science*, vol. 298, pp. 1107–1112, Aug 2020.

[15] D. K. Owens and R. C. Wendt, "Estimation of the surface free energy of polymers," *Journal of Applied Polymer Science*, vol. 13, no. 8, pp. 1741–1747, 1969.

[16] W. Rabel, "Einige aspekte der benetzungstheorie und ihre anwendung auf die untersuchung und veränderung der oberflächeneigenschaften von polymeren," *Farbe und Lack*, vol. 77, no. 10, pp. 997–1005, 1971.

[17] D. Kaelble, "Dispersion-polar surface tension properties of organic solids," *The Journal of Adhesion*, vol. 2, no. 2, pp. 66–81, 1970.

[18] R. J. Good and C. J. van Oss, *The Modern Theory of Contact Angles and the Hydrogen Bond Components of Surface Energies*, pp. 1–27. Boston, MA: Springer US, 1992.

[19] I. Hughes and T. Hase, *Measurements and Their Uncertainties: A Practical Guide to Modern Error Analysis*. OUP Oxford, 2010.

[20] D. Tabor and R. H. S. Winterton, "Surface forces: Direct measurement of normal and retarded van der waals forces," *Nature*, vol. 219, pp. 1120–1121, Sep 1968.

[21] D. Tabor and R. H. S. Winterton, "The direct measurement of normal and retarded van der waals forces," *Proceedings of the Royal Society of London. A. Mathematical and Physical Sciences*, vol. 312, no. 1511, pp. 435–450, 1969.

[22] J. Israelachvili, "Thin film studies using multiple-beam interferometry," *Journal of Colloid and Interface Science*, vol. 44, no. 2, pp. 259–272, 1973.

[23] J. Israelachvili, Y. Min, M. Akbulut, A. Alig, G. Carver, W. Greene, K. Kristiansen, E. Meyer, N. Pesika, K. Rosenberg, and H. Zeng, "Recent advances in the surface forces apparatus (SFA) technique," *Reports on Progress in Physics*, vol. 73, p. 036601, jan 2010.

[24] E. Kumacheva, “Interfacial friction measurement in surface force apparatus,” *Progress in Surface Science*, vol. 58, no. 2, pp. 75–120, 1998.

[25] A. Tonck, S. Bec, D. Mazuyer, J.-M. Georges, and A. A. Lubrecht, “The école centrale de lyon surface force apparatus: An application overview,” *Proceedings of the Institution of Mechanical Engineers, Part J: Journal of Engineering Tribology*, vol. 213, pp. 353–361, May 1999.

[26] J. N. Connor and R. G. Horn, “Extending the surface force apparatus capabilities by using white light interferometry in reflection,” *Review of Scientific Instruments*, vol. 74, no. 11, pp. 4601–4606, 2003.

[27] K. A. Schwenzfeier, A. Erbe, P. Bilotto, M. Lengauer, C. Merola, H.-W. Cheng, L. L. E. Mears, and M. Valtiner, “Optimizing multiple beam interferometry in the surface forces apparatus: Novel optics, reflection mode modeling, metal layer thicknesses, birefringence, and rotation of anisotropic layers,” *Review of Scientific Instruments*, vol. 90, no. 4, p. 043908, 2019.

[28] J. N. Israelachvili and D. Tabor, “Measurement of van der waals dispersion forces in the range 1.4 to 130 nm,” *Nature Physical Science*, vol. 236, pp. 106–106, Apr 1972.

[29] L. L. E. Mears and M. Valiner, *Soft Matter and Biomaterials on the Nanoscale*, ch. 2. World Scientific, 2020.

[30] J. Lachaux, H. Salmon, F. Loisel, N. Arouche, I. Ochoa, L. L. Fernandez, G. Uzan, O. Mercier, T. Veres, and E. Roy, “Soft thermoplastic elastomer for easy and rapid spin-coating fabrication of microfluidic devices with high hydrophilization and bonding performances,” *Advanced Materials Technologies*, vol. 4, no. 2, p. 1800308, 2019.

[31] G. Ovejero, P. Pérez, M. Romero, I. Díaz, and E. Díez, “Sebs triblock copolymer–solvent interaction parameters from inverse gas chromatography measurements,” *European Polymer Journal*, vol. 45, no. 2, pp. 590–594, 2009.

[32] E. Roy, J.-C. Galas, and T. Veres, “Thermoplastic elastomers for microfluidics: Towards a high-throughput fabrication method of multilayered microfluidic devices,” *Lab Chip*, vol. 11, pp. 3193–3196, 2011.

[33] J. Davis, *Corrosion: Understanding the Basics.* ASM International, 2000.

[34] R. Revie, *Corrosion and Corrosion Control: An Introduction to Corrosion*

Science and Engineering. Wiley, 2008.

[35] P. Vanysek, "Electrochemical series," *CRC handbook of chemistry and physics*, vol. 87, 1998.

[36] E. Hornbogen, H. Warlimont, and B. Skrotzki, *Metalle: Struktur und Eigenschaften der Metalle und Legierungen*. Springer Berlin Heidelberg, 2019.

[37] H. Tamura, "The role of rusts in corrosion and corrosion protection of iron and steel," *Corrosion Science*, vol. 50, no. 7, pp. 1872–1883, 2008.

[38] B. Sun, X. Zuo, X. Cheng, and X. Li, "The role of chromium content in the long-term atmospheric corrosion process," *npj Materials Degradation*, vol. 4, p. 37, Nov 2020.

[39] S. Jiang, F. Chai, H. Su, and C. Yang, "Influence of chromium on the flow-accelerated corrosion behavior of low alloy steels in 3.5% nacl solution," *Corrosion Science*, vol. 123, pp. 217–227, 2017.

[40] D. Cubicciotti, "Potential-ph diagrams for alloy-water systems under lwr conditions," *Journal of Nuclear Materials*, vol. 201, pp. 176–183, 1993.

[41] R. G. Bates and J. B. Macaskill, "Standard potential of the silver-silver chloride electrode," *Pure and Applied Chemistry*, vol. 50, no. 11-12, pp. 1701–1706, 1978.

[42] R. T. Foley, "Role of the Chloride Ion in Iron Corrosion," *Corrosion*, vol. 26, pp. 58–70, 01 2013.

[43] G. K. Glass and N. R. Buenfeld, "Chloride-induced corrosion of steel in concrete," *Progress in Structural Engineering and Materials*, vol. 2, no. 4, pp. 448–458, 2000.

[44] L. Jinlong, L. Tongxiang, and W. Chen, "Surface enriched molybdenum enhancing the corrosion resistance of 316l stainless steel," *Materials Letters*, vol. 171, pp. 38–41, 2016.

[45] P.-J. Cunat, "Alloying elements in stainless steel and other chromium-containing alloys," *Euro Inox*, vol. 2004, pp. 1–24, 2004.

[46] L. Murtomäki, T. Kallio, R. Lahtinen, and M. Ikonen, "Fundamental electrochemistry." `https://mycourses.aalto.fi/mod/book/view.php?id=388663&chapterid=1751`, Jan 2018. Accessed: 2022-09-06.

[47] R. Thomas, *Practical Guide to ICP-MS: A Tutorial for Beginners, Third Edition*. CRC Press, 2013.

[48] O. Kasian, S. Geiger, K. J. Mayrhofer, and S. Cherevko, “Electrochemical online icp-ms in electrocatalysis research,” *The Chemical Record*, vol. 19, no. 10, pp. 2130–2142, 2019.

[49] E. Huang, A. Skoufis, T. Denning, J. Qi, R. R. Dagastine, R. F. Tabor, and J. D. Berry, “Opendrop: Open-source software for pendant drop tensiometry & contact angle measurements,” *Journal of Open Source Software*, vol. 6, no. 58, p. 2604, 2021.

[50] Dejan, “Arduino brushless motor control tutorial ESC | BLDC.” `https://howtomechatronics.com/tutorials/arduino/arduino-brushless-motor-control-tutorial-esc-bldc/`. Accessed: 2022-07-27.

[51] Scientific Polymer Products Inc., “Refractive index of polymers by index.” `https://scipoly.com/technical-library/refractive-index-of-polymers-by-index/`. Accessed: 2022-07-27.

[52] V. Wieser, P. Bilotto, U. Ramach, H. Yuan, K. Schwenzfeier, H.-W. Cheng, and M. Valtiner, “Novel in situ sensing surface forces apparatus for measuring gold versus gold, hydrophobic, and biophysical interactions,” *Journal of Vacuum Science & Technology A*, vol. 39, no. 2, p. 023201, 2021.

[53] Schwenzfeier, K. personal communication.

[54] LLE Mears. personal communication.

[55] D. Dworschak, H.-W. Cheng, C.-S. Ku, C.-Y. Chiang, C.-H. Lin, and M. Valtiner, “Comparison of elemental resolved non-confined and restricted electrochemical degradation of nickel base alloys,” *Corrosion Science*, vol. 190, p. 109629, 2021.

[56] D. Dworschak, C. Brunnhofer, and M. Valtiner, “Photocorrosion of zno single crystals during electrochemical water splitting,” *ACS Applied Materials & Interfaces*, vol. 12, pp. 51530–51536, Nov 2020.

[57] F. Clauss, *Solid Lubricants and Self-Lubricating Solids*. Elsevier Science, 2012.

[58] L. Kalchgruber, “Komplementäre experimentelle und theoretische Untersuchungen zur Optimierung einer elektrochemischen ICP-MS Durch-

flusszelle," Master's thesis, Technische Universität Wien, 2020. reposiTUm. https://doi.org/10.34726/hss.2020.78567.

[59] OriginLab Corporation, "Smoothing." `https://www.originlab.com/doc/origin-help/smoothing`. Accessed: 2022-07-27.

[60] R. Akbari and C. Antonini, "Contact angle measurements: From existing methods to an open-source tool," *Advances in Colloid and Interface Science*, vol. 294, p. 102470, 2021.

[61] J. F. Malone, C. M. Murray, M. H. Charlton, R. Docherty, and A. J. Lavery, "X-H$\cdots\pi$ (phenyl) interactions theoretical and crystallographic observations," *J. Chem. Soc., Faraday Trans.*, vol. 93, pp. 3429–3436, 1997.

[62] Y. Gu, T. Kar, and S. Scheiner, "Fundamental properties of the CH···O interaction: is it a true hydrogen bond?," *Journal of the American Chemical Society*, vol. 121, pp. 9411–9422, Oct 1999.

[63] T. van Mourik and F. van Duijneveldt, "Ab initio calculations on the C-H—O hydrogen-bonded systems CH_4-H_2O, CH_3NH_2-H_2O and $CH_3NH_3^+$-H_2O," *Journal of Molecular Structure: THEOCHEM*, vol. 341, no. 1, pp. 63–73, 1995.

[64] J. J. Novoa, B. Tarron, M. Whangbo, and J. M. Williams, "Interaction energies associated with short intermolecular contacts of C–H bonds. ab initio computational study of the C–H$\cdots$O contact interaction in $CH_4\cdots OH_2$," *The Journal of Chemical Physics*, vol. 95, no. 7, pp. 5179–5186, 1991.

[65] M. M. Szczęśniak, G. Chałasiński, S. M. Cybulski, and P. Cieplak, "Ab initio study of the potential energy surface of CH_4-H_2O," *The Journal of Chemical Physics*, vol. 98, no. 4, pp. 3078–3089, 1993.

A. Adhesion Appendix

A.1. OWRK diagram

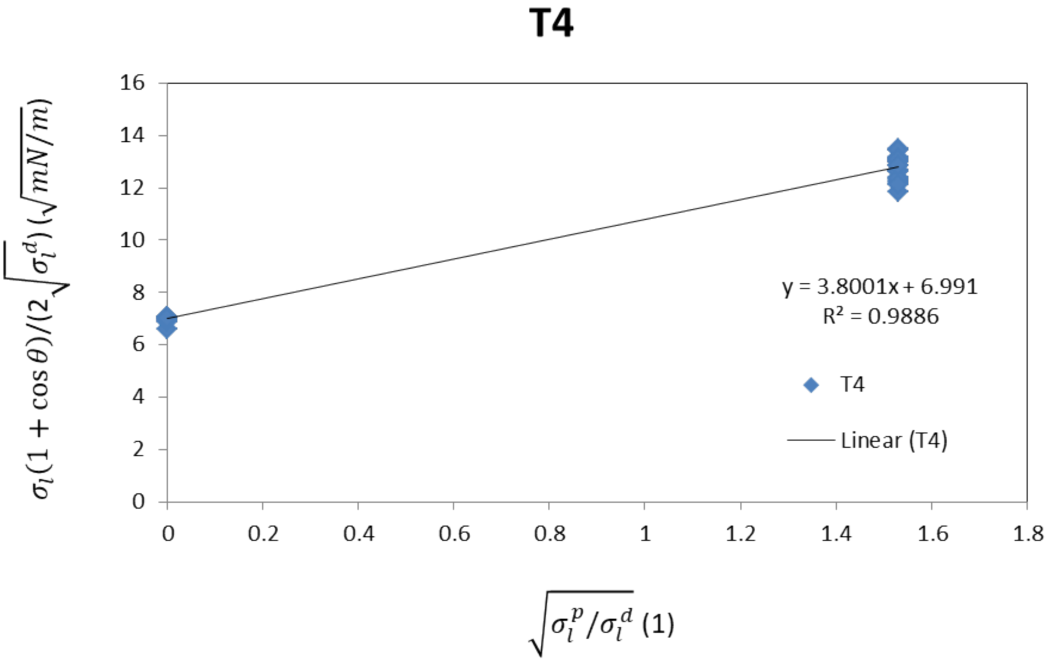

Figure 30: Diagram for evaluation with OWRK method for the T4 sample. Point cluster at x=0 is diiodmethane, at x=1.5 is water. Variation in the diiodmethane point cluster is much less influential because it is masked by the cos-function

A.2. Contact angle data

Table 11: Contact angles for diiodmethane on 2 steel platelets (a and b) of each sample type, averaged across four angles recorded in different orientations of the same droplet; 3 repeat cycles; raw data for the OWRK evaluation.

Name	**a1**	**b1**	**a2**	**b2**	**a3**	**b3**
T1	13.9	13.0	13.0	12.2	13.8	16.6
T2	31.5	27.8	27.4	26.5	28.9	25.8
T3	19.7	18.5	20.6	20.5	17.7	19.5
T4	13.6	22.0	14.6	15.6	12.9	14.0
T5	12.7	18.4	16.1	14.6	14.4	13.6
P2	32.8	28.8	31.5	29.6	30.3	29.2
P3	26.4	26.6	28.1	31.0	28.6	28.7
P4	27.0	28.2	26.8	26.9	23.2	25.6
P5	28.2	28.7	29.1	32.2	26.2	27.2
REF	23.1	26.5	26.2	23.6	20.8	21.0

Table 12: Contact angles for water on 2 steel platelets (a and b) of each sample type, averaged across four angles recorded in different orientations of the same droplet; 3 repeat cycles; raw data for the OWRK evaluation.

Name	**a1**	**b1**	**a2**	**b2**	**a3**	**b3**
T1	54.3	53.1	52.6	54.1	54	55.3
T2	60.1	58.4	57.4	56.1	62.7	59.0
T3	53.6	51.9	54.6	56.4	50.4	53.7
T4	46.5	55.1	46.3	50.2	49.1	52.4
T5	52.1	51.8	46.9	51.5	47.3	52.1
P2	*	*	*	*	*	*
P3	60.9	60.2	56.6	59.1	61.5	57.6
P4	58.1	53.6	58.2	56.6	53.9	54.8
P5	60.0	58.7	55.7	60.5	62.2	64.5
REF	44.8	45.9	44.4	41.4	42.4	44.7

Table 13: Contact angles for water on 2 steel platelets (a and b) of the same sample type, averaged across four angles recorded in different orientations of the same droplet; 3 repeat cycles; sample P2; raw data for the OWRK evaluation.

Name	**a1**	**b1**	**a2**	**b2**	**a3**	**b3**
P2	68.4	71.9	72.9	63.5	55.4	58.2
	71.7	61.2	55.3	55.7	58.3	55.8
	57.6	53.6	53.9	49.8	52.9	49.5

A.3. Contact angle missing error bars

Using the mathematical instrument of linear regression here is questionable in the first place and an error calculated from a linear regression through two point clusters, stemming from two "ideal" data points if there were no error, is consequently meaningless. Rather, splitting of these two "ideal" data points into point clusters of the same x-, but different y-values with significant variation should be interpreted as the linear model not fitting the experimental data, as a statistical test for linearity will attest to. Strictly speaking the linear model should not be used on this data at all and any errors calculated from a linear fit through the data is at best a lower bound, at worst completely devoid of meaning.

Even if a meaningful error could be calculated, comparing it to the original experiment by Berndorf would be of limited merit, as the averaging over four angles necessitates an error progression calculation that was not needed with Berndorf's data.

A.4. Arduino Code

The following code was adopted from [50].

```
/*Arduino Brushless Motor Control by Dejan, https://howtomechatronics.com */

# include <Servo.h>

Servo ESC; // create servo object to control the ESC

int potValue; // value from the analog pin

void setup()

// Attach the ESC on pin 9

ESC.attach(9,1000,2000); // (pin, min pulse width, max pulse width in microseconds)

void loop()

potValue = analogRead(A0); // reads the value of the potentiometer (value between 0 and 1023)

potValue = map(potValue, 0, 1023, 0, 180); // scale it to use it with the servo library (value between 0 and 180)

ESC.write(potValue); // Send the signal to the ESC
```

A.5. SEBS Refractive Index

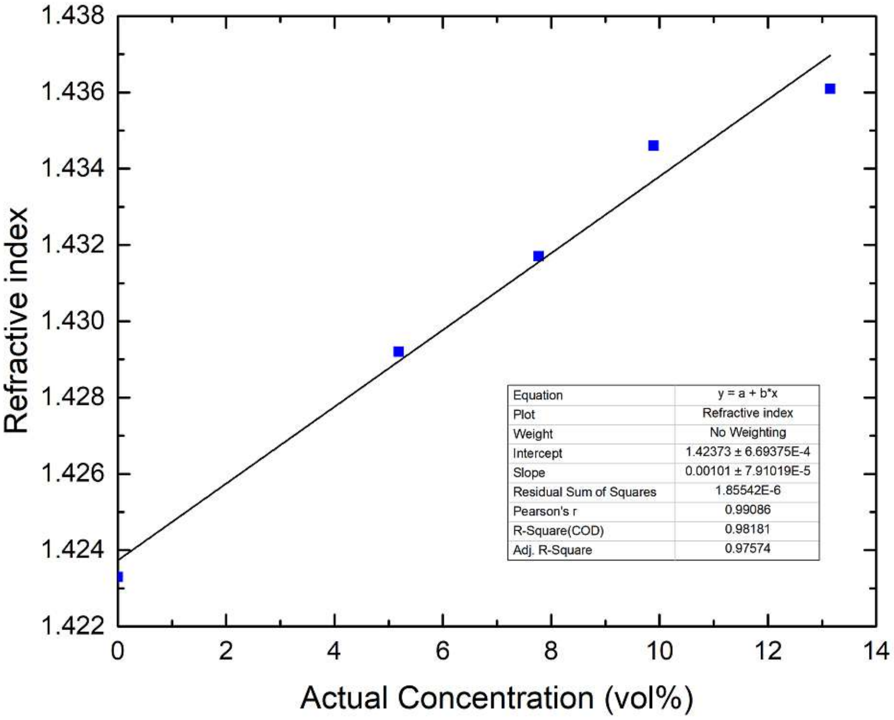

Equation	y = a + b*x
Plot	Refractive index
Weight	No Weighting
Intercept	1.42373 ± 6.69375E-4
Slope	0.00101 ± 7.91019E-5
Residual Sum of Squares	1.85542E-6
Pearson's r	0.99086
R-Square(COD)	0.98181
Adj. R-Square	0.97574

Figure 31: Refractive index of SEBS solutions in cyclohexane; 100% SEBS extrapolated from this data.

A.6. SFA Calibration

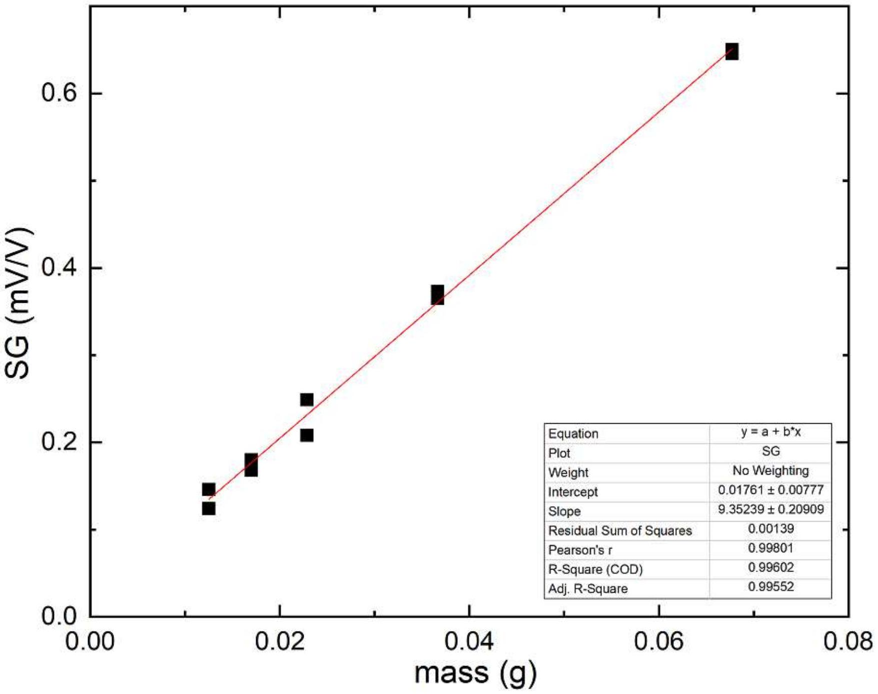

Equation	y = a + b*x
Plot	SG
Weight	No Weighting
Intercept	0.01761 ± 0.00777
Slope	9.35239 ± 0.20909
Residual Sum of Squares	0.00139
Pearson's r	0.99801
R-Square (COD)	0.99602
Adj. R-Square	0.99552

Figure 32: SFA calibration

A.7. SFA Long Time Experiment

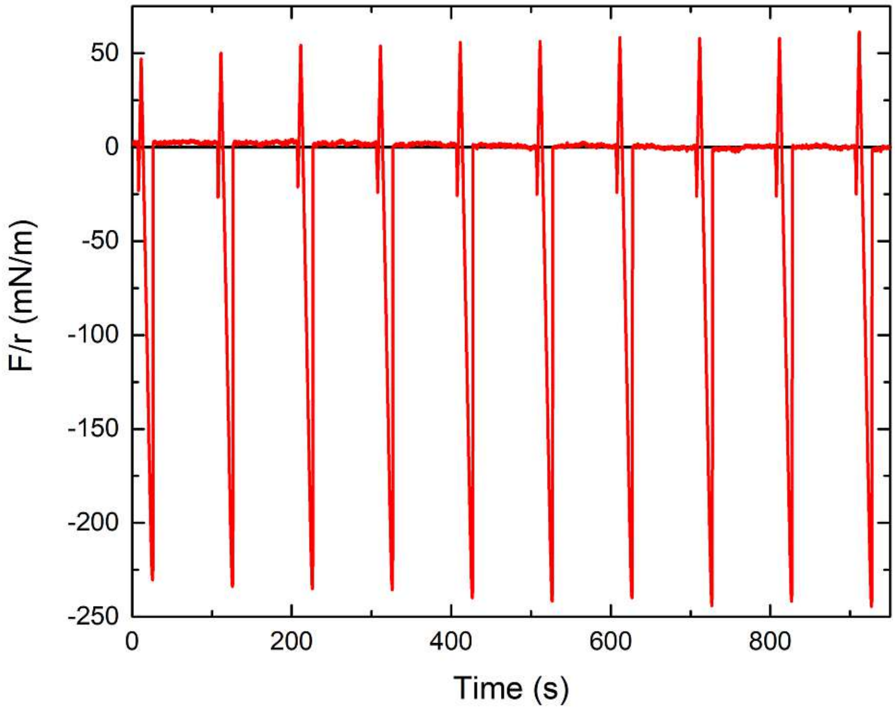

Figure 33: Force-time graph with 10 repeat cycles on the REF-steel sample.

B. Corrosion Appendix

B.1. Calibrations

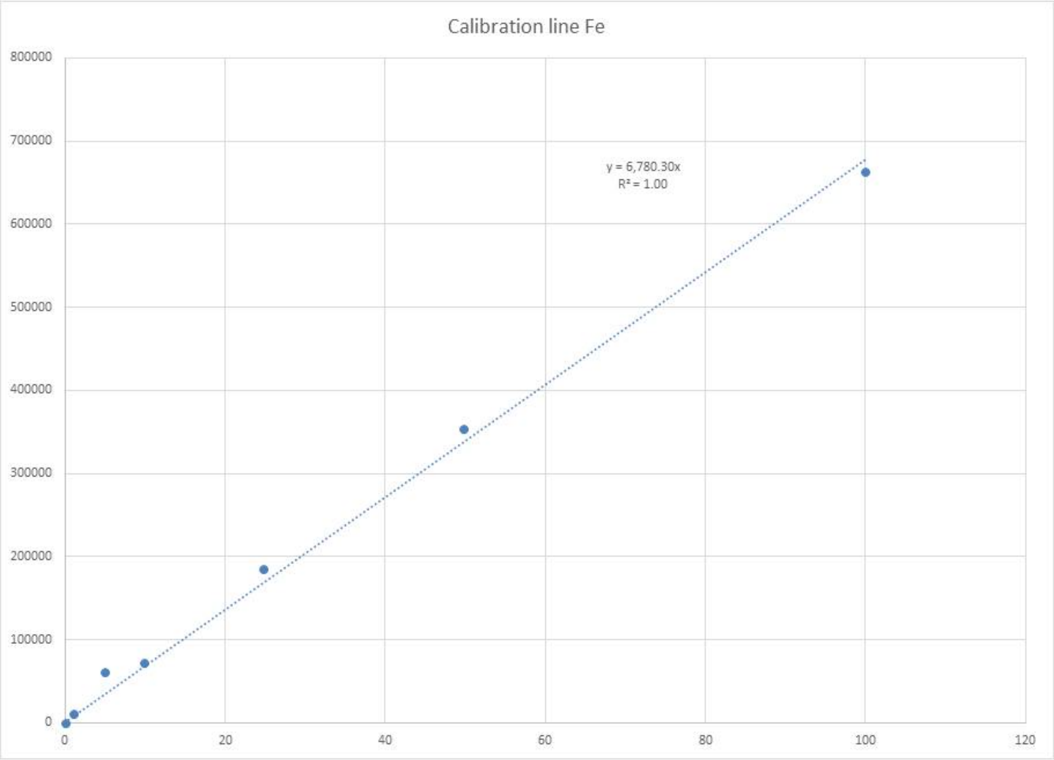

Figure 34: ICP-MS calibration line for Fe.

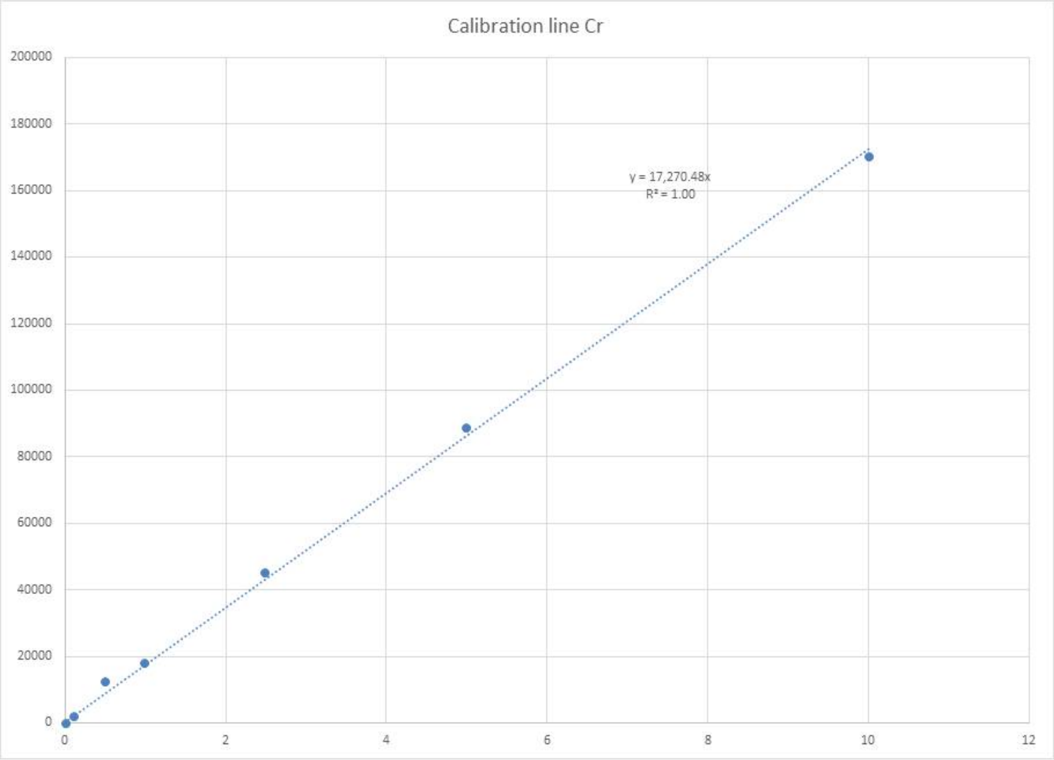

Figure 35: ICP-MS calibration line for Cr.

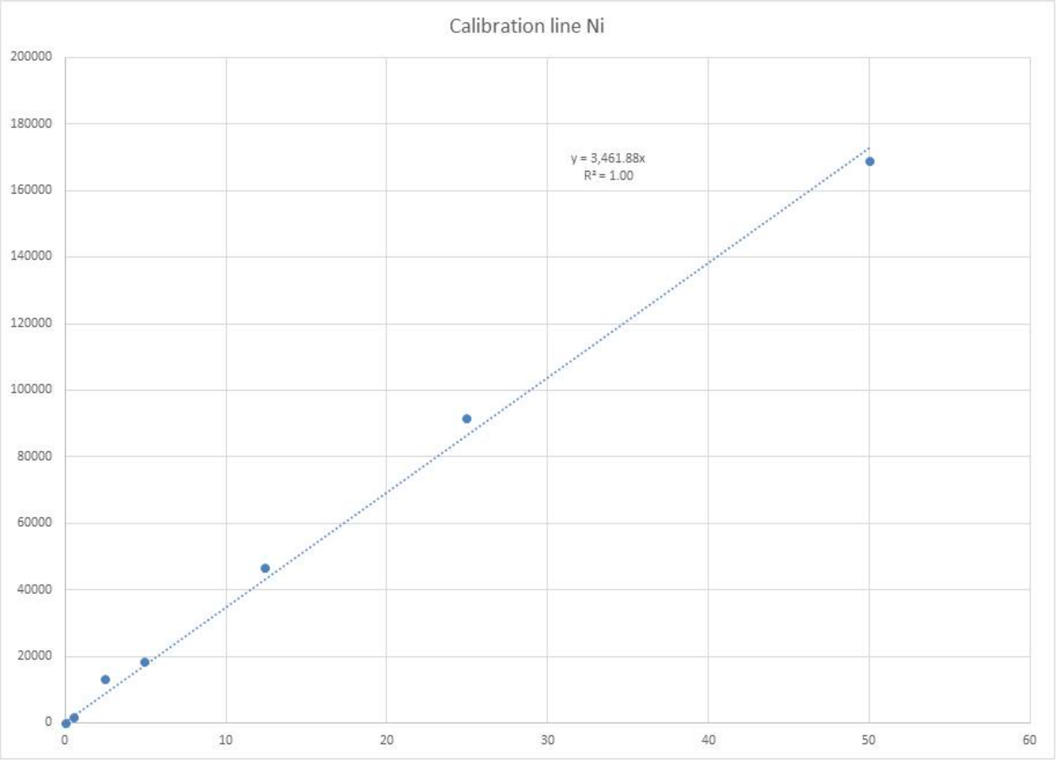

Figure 36: ICP-MS calibration line for Ni.

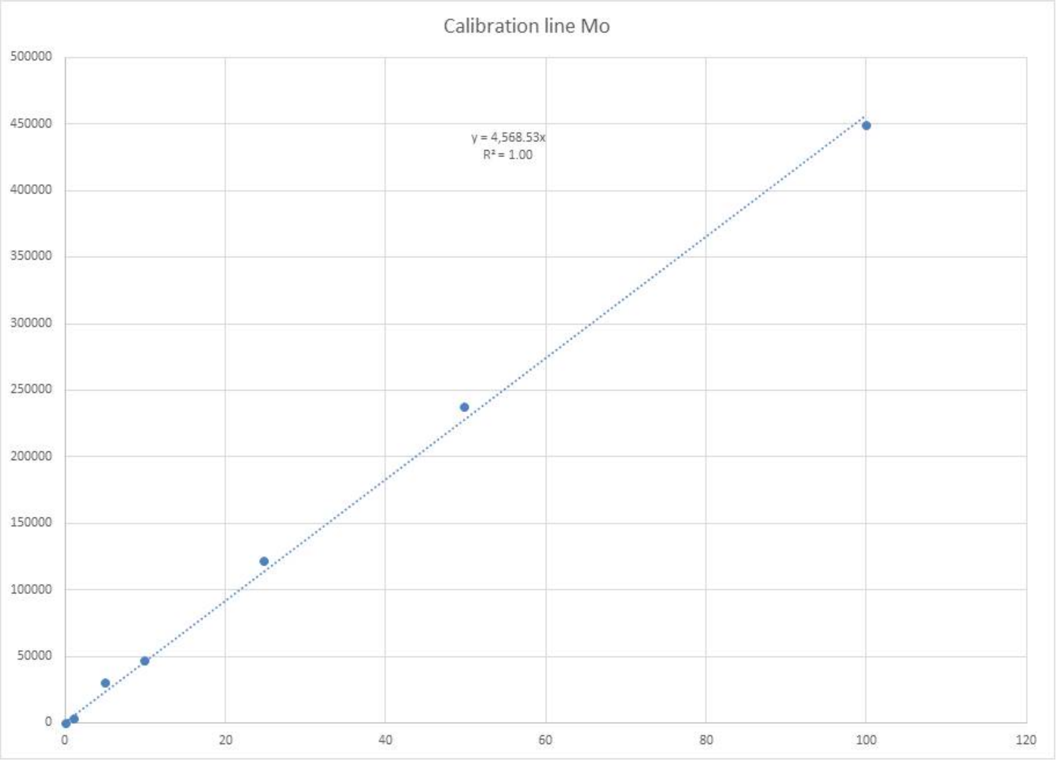

Figure 37: ICP-MS calibration line for Mo.

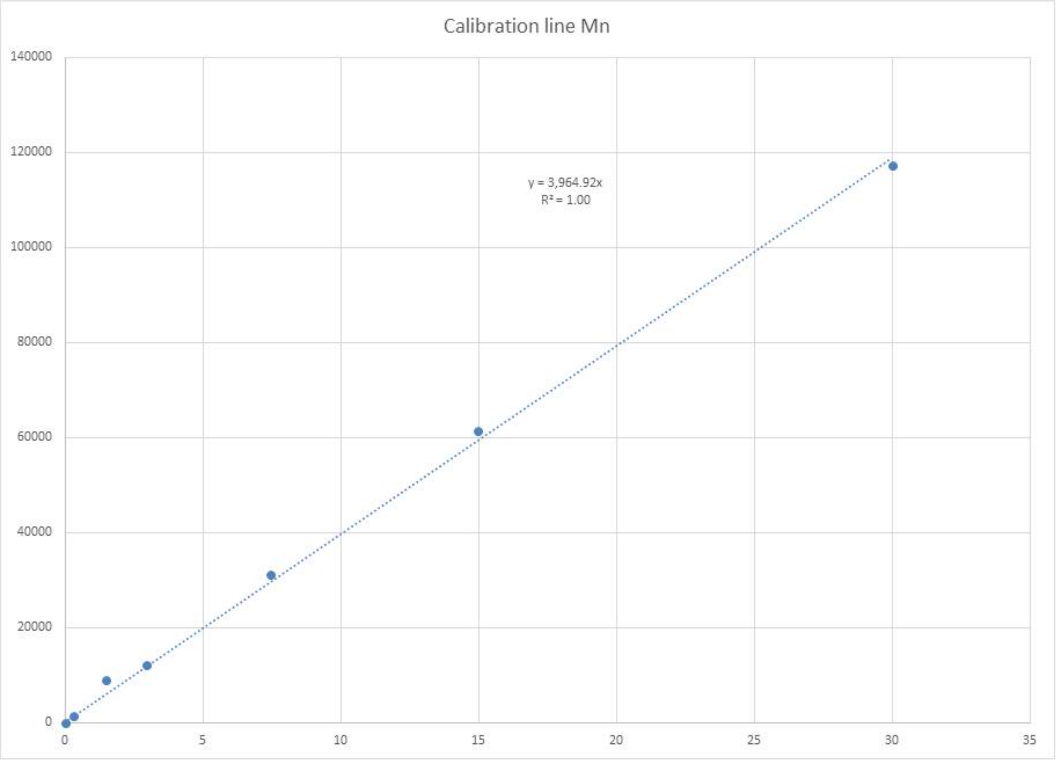

Figure 38: ICP-MS calibration line for Mn.

B.2. Mass Flows and OCPs

The following Table 14 gives an overview over the rounded mass flows in g/s and OCPs in V for the individual ICP-MS experiments. Only experiments that were also considered for half-life time calculation are listed (without major artifacts) plus the FeCr4 run.

Table 14: Mass flows and OCPs for ICP-MS experiments.

Experiment	**Sample**	**mass flow (g/s)**	**OCP (V)**
105_1	FeCr4	0.0074	-
108_1	B1	0.0078	-0.25
109_1	B2	0.0080	-0.16
110_1	G1	0.0075	-0.28
111_1	G1	0.0049	-0.22
112_1	B1	0.0009	-0.5
115_1	FeCr12	0.0063	-0.31
116_1	FeCr16	0.0062	-0.44
120_1	FeCr17.5	0.0059	-0.52
123_1	FeCr17.5	0.0070	-0.49

B.3. Unsmoothed ICP-MS Graphs

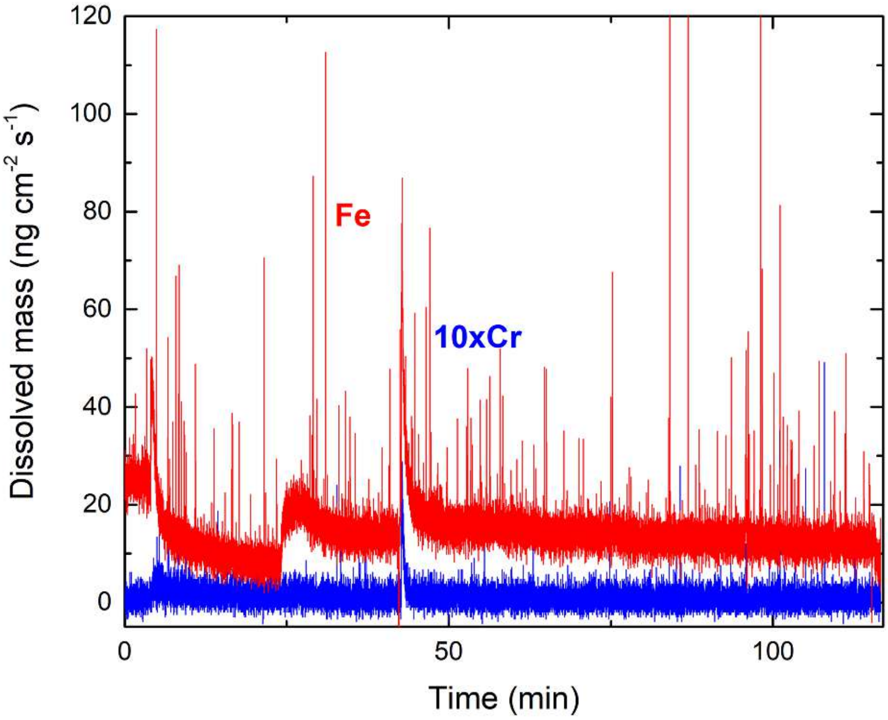

Figure 39: FeCr17.5 unsmoothed for reference; compare to Figure 24.

B.4. Dissolution Ratios

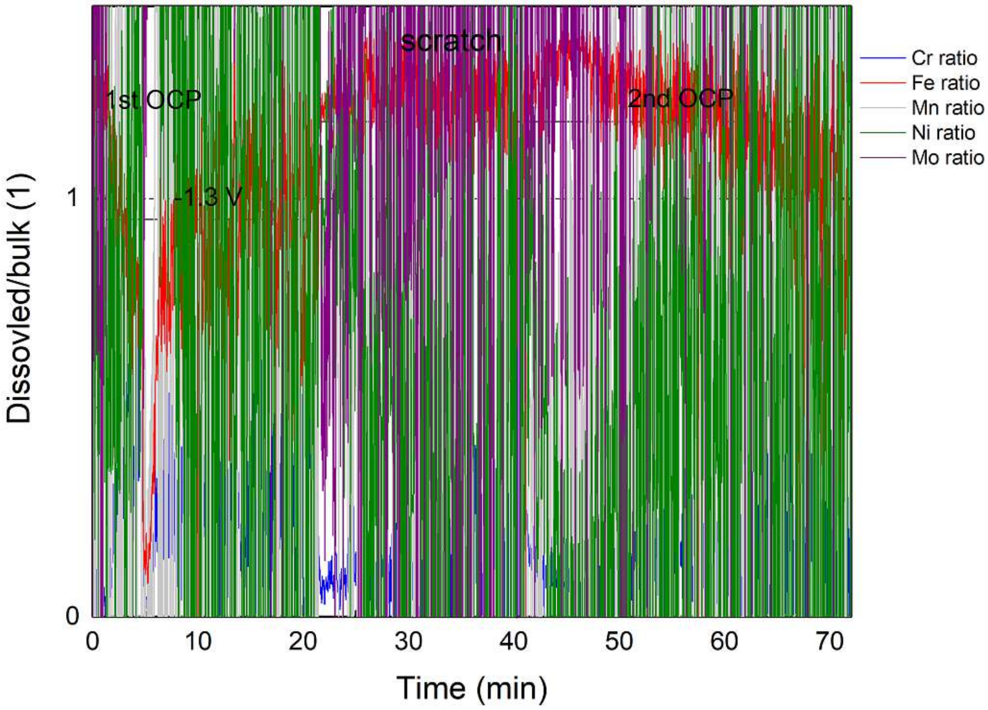

Figure 40: Uninterpretable dissolution ratio plot for the multi-element sample G1.